Human iPSC-based neurodevelopmental models of globoid cell leukodystrophy uncover patient- and cell type-specific disease phenotypes

Elisabeth **Mangiameli**[1], Anna **Cecchele**[1], Francesco **Morena**[2], Francesca **Sanvito**[3], Vittoria **Matafora**[4], Angela **Cattaneo**[4], Lucrezia **Della Volpe**[1], Daniela **Gnani**[1], Marianna **Paulis**[5,6], Lucia **Susani**[5,6], Sabata **Martino**[2], Raffaella **Di Micco**[1], Angela **Bachi**[4], and Angela **Gritti**[1]

1. San Raffaele Telethon Institute for Gene Therapy (SR-Tiget), IRCCS San Raffaele Scientific Institute, Via Olgettina 60, 20132 Milan, Italy
2. Department of Chemistry, Biology and Biotechnology, University of Perugia, Via del Giochetto, 06123 Perugia, Italy
3. Pathology Unit, IRCCS San Raffaele Scientific Institute, Via Olgettina 60, 20132 Milan, Italy
4. IFOM-FIRC Institute of Molecular Oncology, Via Adamello 16, 20139 Milan, Italy
5. Humanitas Clinical and Research Center-IRCCS, Rozzano, Milan, Italy.
6. National Research Council (CNR)-IRGB/UOS of Milan, Milan, Italy.

Correspondence:

Angela Gritti, San Raffaele Telethon Institute for Gene Therapy (SR-Tiget), IRCCS San Raffaele Scientific Institute, Via Olgettina 60, 20132 Milan, Italy; e-mail: gritti.angela@hsr.it

Words/characters counting (with spaces):

Title: 118 characters

Running title: 26 characters

Summary: 254 words

Text (including methods and figure legends): 11,184 words

Main Figures: 7

Supplementary Figures and Data: 1 table, 9 figures

References: 104

Summary

Globoid Cell Leukodystrophy (GLD, or Krabbe disease) is a rare lysosomal storage disease caused by inherited deficiency of β-galactocerebrosidase (GALC). The build-up of galactosylsphingosine (psychosine) and other undegraded galactosylsphingolipids in the nervous system causes severe demyelination and neurodegeneration. The molecular mechanisms of GLD are poorly elucidated in neural cells and whether murine systems recapitulate critical aspects of the human disease is still to be defined.

Here, we established a collection of GLD patient-specific induced pluripotent stem cell (iPSC) lines. We differentiated iPSCs from two patients (bearing different disease-causing mutations) into neural progenitors cells (NPCs) and their neuronal/glial progeny, assessing the impact of GALC deficiency and lentiviral vector-mediated GALC rescue/overexpression by means of phenotypic, biochemical, molecular, and lipidomic analysis. We show a progressive increase of psychosine during the differentiation of GLD NPCs to neurons and glia. We report an early and persistent impairment of oligodendroglial and neuronal differentiation in GLD cultures, with peculiar differences observed in the two GLD lines. GLD cells display a global unbalance of lipid composition during the iPSC to neural differentiation and early activation of cellular senescence, depending on the disease-causing mutation. Restoration of GALC activity normalizes the primary pathological hallmarks and partially rescues the differentiation program of GLD NPCs.

Our results suggest that multiple mechanisms besides psychosine toxicity concur to CNS pathology in GLD and highlight the need of a timely regulated GALC expression for proper lineage commitment and differentiation of human NPCs. These findings have important implications for establishing tailored gene therapy strategies to enhance disease correction in GLD.

Keywords

Pluripotent stem cells, leukodystrophy, Krabbe disease, gene therapy, neural progenitors, oligodendrocytes, senescence.

Running title

Human iPSC-based models of GLD

Introduction

Globoid Cell Leukodystrophy (GLD, or Krabbe disease) is a rare lysosomal storage disorder (LSD) caused by inherited deficiency of β-galactocerebrosidase (GALC), a key enzyme in the catabolism of galactosphingolipids, e.g. galactosylceramide and galactosylsphingosine (psychosine) (Suzuki and Suzuki, 1970). The infantile forms are characterized by relentless demyelination and neurodegeneration of the central and peripheral nervous system (CNS, PNS). Allogeneic hematopoietic stem/progenitor cell (HSPC) transplant - the only therapeutic option for GLD infants - provides a functional GALC enzyme to the affected organs through the engraftment of HSPC-derived myeloid progeny. However, it fails to fully correct the severe CNS pathology, even if performed at the asymptomatic stage (Allewelt et al., 2016), likely because of the insufficient GALC supply provided by HSPC-derived microglia in the brain and/or modest metabolic correction of endogenous cells. *In vivo* and *ex vivo* gene therapy (GT) approaches using lentiviral vectors (LV) and adeno-associated vectors (AAV) benefit GLD animal models (Bradbury et al., 2018; Gentner et al., 2010; Lattanzi et al., 2010, 2014; Lin et al., 2005; Meneghini et al., 2016; Rafi et al., 2015; Ricca et al., 2015; Ungari et al., 2015). The advantage of *ex vivo* GT with LV-modified HSPCs in infants affected by metachromatic leukodystrophy (MLD) – a similar LSD (Biffi et al., 2013; Sessa et al., 2016), suggests that a similar approach might be translated to GLD. Still, the obstacles in reaching safe, widespread and stable expression of therapeutic GALC levels in the human CNS limits the clinical development of these GT strategies to GLD.

Studies in GLD mice suggest that a modest accumulation of psychosine impairs CNS and PNS development from neural progenitor cells (NPCs) (Castelvetri et al., 2011; Santambrogio et al., 2012; Teixeira et al., 2014). Then, psychosine accumulates in GLD neurons and glial cells until reaching a threshold that triggers cytotoxicity. Besides the effects exerted on myelin and axons, psychosine and other substrates in the GALC-related sphingolipid pathway (Hannun and Obeid, 2017) directly or indirectly affect glial and neuronal cell homeostasis interfering with lipid content and distribution (Giri et al., 2006; White et al., 2009), altering proteostasis network (Pellegrini et al., 2019), promoting apoptosis (Jatana et al., 2002), lysosomal dysfunction (Folts et al., 2016; Samie and Xu, 2014), and autophagy (Del Grosso et al., 2019). Growing evidence points to a previous underestimated association between lysosomal dysfunction, protein misfolding/aggregation, lipid unbalance, and senescence in multiple organisms and cell types (Buratta et al., 2017; Irahara-Miyana et al., 2018; Lee et al., 2014; Lizardo et al., 2017; Smith et al., 2014; Trayssac et al., 2018). Also, recent observations implicate NPCs and oligodendroglial progenitor cells (OPCs) senescence in the pathogenesis of neurodegenerative disorders with protein aggregation (Zhang et al., 2019) and neuroinflammatory demyelinating disorders (Nicaise et al., 2019), providing a strong

rationale for investigating the potential implication of these processes in GLD. Altogether, these complex and yet poorly elucidated events may contribute to the multifaceted aspects of GLD pathology and explain the modest efficacy of conventional or experimental therapies in correcting CNS and PNS damage in GLD animal models and patients (Allewelt et al., 2016; Hawkins-Salsbury et al., 2015; Rafi et al., 2015; Ricca et al., 2015).

More than 100 disease-causing mutations in the human *GALC* gene have been described (Wenger and Luzi, 2014), among which a 30-kb deletion accounts for 40% of pathogenic alleles in the Caucasian population (Rafi et al., 1995). The occurrence of this large gene deletion in homozygosis is associated to the early-onset and most severe disease forms. The genotype-phenotype correlation is less clear for the many missense/nonsense mutations occurring in homozygosis or compound heterozygosis, which may be associated to variable residual GALC activity and severe to mild disease variants (Duffner et al., 2011, 2012; De Gasperi et al., 1996, 1999; Jalal et al., 2012; Tappino et al., 2010). Misfolded GALC proteins evoke different Unfolded Protein Response (UPR) activation (Irahara-Miyana et al., 2018) and show mutation-specific alteration of trafficking to lysosomes and processing (Shin et al., 2016), suggesting the occurrence of pathological cascades that are independent from or act in synergy with primary lipid storage in determining the complex GLD phenotype. Thus, studying the mechanisms linking the primary mutation-specific event(s) to progressive cell dysfunction and death is relevant and requires appropriate experimental models.

Murine, canine and non-human primate models of GLD (Wenger, 2000) have been used to test the safety and efficacy of novel therapies; nevertheless, they fail to fully recapitulate the spectrum of pathological manifestations observed in patients. Also, the most used mouse model (Suzuki, 1983) and non-human primate model of GLD (Borda et al., 2008; Luzi et al., 1997) carry spontaneous mutations that are not found in humans. Conventional GLD human cellular models include patient-specific fibroblasts (Berardi et al., 2014; Gama Sosa et al., 1996; Rafi et al., 1996; Ribbens et al., 2013; Spratley et al., 2016), human hematopoietic cells (Martino et al., 2009), or epithelial cell lines with induced GALC mutations (Lee et al., 2010; Shin et al., 2016) that hardly recapitulate the metabolic and functional features of NPCs and their differentiated progeny. Thus, there is a strong need for human-derived experimental models to explore GLD pathogenesis and test correction strategies.

Human induced pluripotent stem cells (iPSCs) (Yamanaka, 2007) offer a unique tool to analyze the molecular consequences of pathogenic mutations in the context of the genetic background of individual patients. The differentiation of iPSCs in neural cells has boosted CNS disease modelling and therapeutic screening (Shi et al., 2017). Human iPSCs are available from a variety of LSDs (Huang et al., 2012) but there

are no reports describing GLD patient-derived iPSCs.

Here, we established GLD patient-specific iPSC lines as a reliable human model for elucidating GLD pathogenesis and testing the biological efficacy of gene therapy in relevant neural cell types. To this end, we differentiated iPSCs into NPCs and differentiated cells (oligodendrocytes, neurons, and astrocytes) and monitored the appearance/progression of cell type- and patient-specific primary and secondary defects in GLD cells. Finally, we assessed the impact of GALC reconstitution/overexpression (achieved by lentiviral-mediated gene transfer) in reverting the pathological phenotype and its potential impact on the biology of human NPCs and progeny.

Results

GLD iPSCs show undetectable GALC activity and psychosine storage but display normal pluripotency features

We generated iPSCs from fibroblasts of 5 GLD patients with distinct biallelic mutations in the *GALC* gene (homozygous or compound heterozygous) resulting in the infantile form of the disease. Control iPSC lines were generated from fibroblasts of two unrelated normal donors (ND1, adult; ND2, neonatal) and one non-affected relative (ND3, parent of GLD1)(**Table S1**). GALC activity in ND fibroblasts was 2.42 nmol*h/mg (ND1), 3.89 nmol*h/mg (ND2), and 1.56 nmol*h/mg (ND3), while it was below the limit of detection in all GLD fibroblasts, indicating that the mutated GALC proteins have no residual functionality. By using an integration-free, feeder-free microfluidic reprogramming system (Luni et al., 2016) we obtained several iPSC clones from each patient and ND fibroblast line (reprogramming efficiency: 2-53%)(**Figure S1A**). After 6-10 subculturing passages, we randomly selected two clones/line for further analysis (**Figure S1A**). The presence of GALC mutations was verified by PCR analysis and sequencing (**Figure S1B-C**).

We assessed the pluripotency of GLD and ND iPSC clones by RT-PCR **(Figure S1D**) and immunocytochemistry (**Figure 1A**) for the markers NANOG, SOX2, KLF4, OCT4, and TRA1-60. Analysis of endodermal-, mesodermal-, and ectodermal-specific markers in embryoid bodies (**Figure 1B; Figure S1E**) and histological assessment of teratomas (**Figure S1F**) confirmed the ability of GLD and ND iPSCs to differentiate in multiple cell types and tissues both *in vitro* and *in vivo*.

All the GLD iPSC clones displayed undetectable GALC activity (**Figure 1C**) and significant psychosine storage (50- to -100-fold the ND levels) that was absent in parental fibroblasts (**Figure 1D).**

Overall, GLD patient iPSCs showed the primary biochemical GLD hallmarks while retaining normal

155 stem cell properties, justifying their use as human-based GLD model.
156
157 **LV-mediated gene transfer in GLD iPSCs rescues GALC activity and normalizes psychosine storage**
158 We focused on the mutant lines GLD1 and GLD5 (two clones/line) for further characterization and
159 gene transfer studies. GLD1 is homozygous for the large 30 Kb *GALC* gene deletion
160 (c.1161+6532_polyA+9kbdel) producing a truncated protein that lacks the whole coding region for the
161 30kDa subunit and 15% of the coding region for the 50kDa subunit (Luzi et al., 1995; Tappino et al., 2010).
162 GLD5 is homozygous for a missense mutation (c.1657G>A) that is predicted to cause GALC protein
163 misfolding (De Gasperi et al., 1996; Tappino et al., 2010). ND1 and ND2 iPSCs (two clones/lines) were used
164 as controls for all the subsequent experiments (**Table S1, Figure S1A**).
165 We selected ND and GLD iPSC clones with normal karyotype (**Figure S2**) and used these cells within
166 subculturing passages 8-30. To restore GALC activity, we transduced GLD1 and GLD5 iPSC clones using a
167 laboratory grade/scale VSV-pseudotyped third-generation lentiviral vector (LV) encoding for the human
168 (h) *GALC* gene tagged with the Myc peptide under the control of the human phosphoglycerate kinase (PGK)
169 promoter (LV.hGALC) (Meneghini et al., 2016)(**Figure 2A**). Pilot dose-response experiments showed the
170 proficient transduction of iPSC clones at Multiplicity of Infection (MOI)=2 (**Figure S3A**), which was selected
171 to transduce GLD1.1, GLD1.3, GLD5.2, GLD5.6 and ND2.2 iPSC clones in all the following experiments.
172 LV.hGALC-transduced GLD (GLD^{GALC}) and ND (ND^{GALC}) iPSCs showed vector copy number (VCN) ranging
173 from 5 to 15 (**Figure 2B**), significant GALC mRNA (**Figure 2C**) and protein expression (**Figure 2D-E),** and
174 increased enzymatic activity (reaching supraphysiological levels; **Figure 2F**). We observed a clear
175 correlation between VCN, GALC mRNA expression and enzymatic activity (**Figure S2B**).
176 The transgenic GALC enzyme was functional and able to normalize psychosine levels in GLD iPSCs
177 (**Figure 2G**), which do not show other pathological hallmarks related to GALC deficiency (i.e. GalCer
178 accumulation, increased LAMP1 expression – index of lysosomal expansion) (**Figure S3C-D).** Importantly,
179 LV transduction and GALC overexpression did not affect the pluripotency (**Figure S3E**) and proliferation
180 rate (**Figure S3F**) of ND and GLD iPSC clones.
181
182 **GLD and ND iPSC-derived NPCs are generated with similar efficiency and show comparable phenotype**
183 We next assessed the impact of GALC deficiency and LV-mediated GALC restoration in iPSC-
184 derived neural cells. We first differentiated GLD, GLD^{GALC}, ND, and ND^{GALC} iPSCs into NPCs taking advantage
185 of a published protocol (Chambers et al., 2009)(**Figure 3A**). iPSC-NPCs showed downregulation of
186 pluripotency markers (OCT4, NANOG) and upregulation of NPC markers (NESTIN, PAX6, FOXG1), early

neuronal (Doublecortin, DCX) and glial cell (ASCL1) markers **(Figure 3B-C).** We obtained NPCs with similar efficiency from untransduced (UT) and LV.hGALC-transduced GLD and ND iPSCs in multiple rounds of differentiation experiments with the only exception of clone GLD1.3^{GALC}, which consistently displayed abnormal morphology (not shown) and modest PAX6 upregulation as compared to other clones (**Figure 3B**). Based on these observations suggesting incomplete/defective neural induction, we excluded clone GLD1.3^{GALC} from further analysis. All the selected NPC lines stably expanded in culture for 5-6 passages in the presence of neural medium (N2)(**Figure 3D).**

Thus, ND and GLD iPSC-derived NPCs display bona-fide NPC molecular and phenotypic features.

Time- and cell type-dependent transcriptional regulation of GALC expression and activity during iPSC-NPC differentiation to neurons and glia

Myelinating cells and neurons are highly susceptible to psychosine-mediated toxicity, but astrocytes are also affected (Misslin et al., 2017; Potter and Petryniak, 2016). Therefore, we envisaged that differentiation of iPSC-NPCs into mixed neuronal/glial cultures would better model the composite GLD pathology. We adapted a published protocol (Frati et al., 2018) to generate cell populations containing neurons, astrocytes, and oligodendrocytes from ND, GLD, GLD^{GALC}, and ND^{GALC} iPSC-NPCs. Cultures were evaluated at day 0 (d0; NPCs), d7, d14, and d24 of differentiation (**Figure 3E**), to track the time-course GALC expression/activity and the glial/neuronal cell commitment and maturation by means of biochemical and molecular analysis.

The GALC transcript was expressed at low levels in both ND and GLD iPSC clones (GLD1 and GLD5 mutations are not predicted to impact on mRNA transcription) and was upregulated during the neural induction and neuronal/glial differentiation (**Figure 3F**). GALC mRNA expression in GLD^{GALC} and ND^{GALC} iPSCs was constant over time, due to the high and stable expression driven by the constitutive PGK promoter **(Figure 3F).**

ND NPCs and differentiated cultures (d14 and d24) showed comparable GALC enzymatic activity **(Figure 3G).** The supraphysiological (≈10X the normal levels) GALC activity in GLD^{GALC} iPSCs progressively decreased during the neural differentiation to reach physiological levels at d14 and d24, whereas ND^{GALC} differentiated cultures maintained supraphysiological GALC activity (≈3-fold the ND counterpart at d14 and d24) (**Figure 3G**). The stable VCN measured in ND^{GALC} and GLD^{GALC} cultures at different time points of differentiation (**Figure 3H**) rules out the possibility that the decrease in enzymatic activity results from the counter selection of cells harboring high VCN.

Overall these data show that LV-mediated gene transfer ensures (supra)physiological GALC

219 expression and activity in iPSC-NPCs and neuronal/glial progeny, and highlight a stringent transcriptional
220 regulation of GALC activity during the iPSC to neural differentiation.
221
222 **GLD iPSC-NPCs display defective neural and glial differentiation: impact of GALC rescue/overexpression**
223 **on psychosine levels and phenotype.**
224 The altered expression pattern of the master oligodendroglial gene OLIG2 observed in GLD1 and
225 GLD5 cells as compared to ND cells suggest an altered oligodendroglial differentiation program, which was
226 only partially normalized in GLD^{GALC} cultures **(Figure S4A)**. Interestingly, a similar (or even more severe)
227 alteration was observed in ND^{GALC} cultures, in which OLIG2 expression is overall strongly reduced (**Figure**
228 **S4A**). Immunofluorescence and WB analysis showed an early and persistent reduction of oligodendroglia
229 (OLIG2+, APC+ cells; **Figure 4A-B)** and a significant downregulation of OLIG1 protein expression (**Figure**
230 **S4B**; d24) in both GLD1 and GLD5 NPC-derived cultures as compared to the ND counterpart, highlighting
231 a partial phenotypic rescue in GLD^{GALC} cells and a detrimental impact of GALC overexpression in ND cultures
232 (**Figure 4A-B** and **Figure S4B).**
233 GALC deficiency affected neuronal differentiation, with some differences observed in the two GLD
234 lines. The mRNA expression of Doublecortin (DCX), a marker of immature neurons, was reduced in GLD5
235 (but not in GLD1) as compared to ND cells **(Figure S5A).** In line with these results, GLD5 cultures showed a
236 significant time-dependent reduction of TUJ1+ neurons (**Figure 4C-D**) and a decreased and/or delayed
237 TUJ1 and neurofilament (NF)-M protein expression, respectively (**Figure S5B-C).** The major decrease in the
238 expression of acetylated and polyglutamated tubulin and phosphorylated NF observed in GLD5 cultures
239 (d14 and d24; **Figure S6**) further suggested neuronal loss and/or defective neuronal
240 differentiation/maturation. In contrast, GLD1 cultures displayed normal proportions of neuronal cells
241 (**Figure 4C-D)** and normal expression of neuronal proteins (**Figure S5B-C)**. The quantitative and qualitative
242 neuronal defects observed in GLD5 cultures were rescued in differentiated GLD^{GALC} cultures (**Figure 4C,**
243 **Figure S5B-C**), which also showed an early upregulation of NF-M protein as compared to the ND cultures
244 and untransduced counterparts (**Figure S5C),** suggesting an accelerated neuronal differentiation
245 associated to GALC overexpression. Similarly to what observed in oligodendroglial cells, GALC
246 overexpression negatively affected the pattern of gene and protein expression (**Figure S5, S6**), as well as
247 the number and morphology of ND neurons (**Figure 4C-D)**.
248 Astroglia is the less represented and most variable cell population in both ND and GLD
249 differentiated cultures, with no clear differences related to GALC deficiency, as shown by glial fibrillary
250 acidic protein (GFAP) gene expression analysis (**Figure S7A**), WB analysis (**Figure S7B**), and IF **(Figure 4C-D**

and **Figure S7C**; 3-15% of GFAP+ cells on the total cells at d24).

Interestingly, both GALC deficiency (GLD cultures) and forced GALC expression (GLD^{GALC} and ND^{GALC} cultures) were associated to higher percentages of cells that stained negative for the selected lineage-specific markers **(Figure S7C).**

Psychosine levels were low in GLD iPSC-NPCs and increased during differentiation, to reach ≈8 (GLD1) and ≈30 fold (GLD5) the normal levels at d24 (**Figure 5A**). The psychosine build up was not associated to a significant increase of apoptotic cells (cleaved caspase 3+; **Figure 5B**) or to enhanced phospholipase A2 (PLA2) activity (**Figure 5C**), which has been associated to psychosine-induced apoptotic cell death (Misslin et al., 2017). Psychosine levels were normalized in $GLD1^{GALC}$ cultures and strongly reduced in $GLD5^{GALC}$ cultures (≈2-fold the normal), in line with the enzymatic reconstitution. We observed moderate enlargement of lysosomal vesicles (Lysotracker assay) (**Figure 5D**) in GLD1 NPCs, which was normalized in $GLD1^{GALC}$ cultures. LAMP1 protein expression was comparable in ND, GLD, and GLD^{GALC} differentiated cultures, while it was increased in GALC-overexpressing ND cells (**Figure 5E**).

Taken together, these data show that: i) GALC deficiency severely impairs the differentiation of hiPSC-derived NPCs into oligodendrocytes and neurons, with cell type- and patient-specific phenotypes; ii) LV-mediated GALC reconstitution in GLD cells reduces psychosine levels and provides partial phenotypic rescue in GLD neural progeny; iii) GALC-overexpressing ND cells display lysosomal expansion and a defective neuronal and glial phenotype, suggesting that a tight regulation of GALC expression is required to ensure proper NPC functionality and preserve multipotency**.**

Early activation of a senescence response in GLD5 iPSC-derived neural cells

Our data suggested a marginal contribution of cell death to the loss of GLD neurons and glial cells. Therefore, we explored whether the altered differentiation programs of GLD NPCs and progeny could be caused by an alteration of proliferative potential. By performing and quantifying Ki67/nestin immunostaining at the different stages of the differentiation protocol, we showed a time-dependent decrease in the percentage of proliferating cells in all ND and GLD cultures, indicating the lineage commitment of iPSC-NPCs, their exit of cell cycle and acquisition of a post-mitotic state (**Figure 6A).** Interestingly, EdU incorporation assay performed at the same time points during differentiation showed an earlier and more drastic drop in the percentage of cells in active S-phase in GLD5 cultures as compared to ND and GLD1 counterparts (**Figure 6B).** This proliferation drop was recovered in $GLD5^{GALC}$ cultures (**Figure 6B**).

282 We next investigated whether the early proliferation arrest highlighted in GLD5 cultures was
283 associated with the establishment of cellular senescence, a biological process characterized by stable
284 growth arrest, accumulation of DNA damage and activation of a pro-inflammatory program collectively
285 known as SASP, senescence-associated secretory phenotype (He and Sharpless, 2017). We detected
286 upregulation of the cell cycle inhibitor p21 protein (**Figure 6C)** and increased nuclear levels of DNA
287 damage response (DDR) markers 53BP1 (**Figure 6D)** and yH2AX **(Figure S8A-B)** as early as d7 post-
288 differentiation. The induction of DDR and p21 was specific of GLD5 cultures, not reported in ND or
289 GLD1 cultures, and was partially rescued by in GLD5^{GALC} cultures. We also observed a dramatic increase
290 in the percentage of Senescence Associated (SA) β-gal positive cells in GLD5 (but not ND or GLD1
291 cultures) with a peak at d7 of differentiation (**Figure 6E**), and variable induction of the SASP pro-
292 inflammatory factors TNF-α and IL1-β (**Figure S8E-F**). These senescence-associated hallmarks were
293 reduced in GLD5^{GALC} cultures.
294 Altogether, our data suggest that GLD5 iPSC-derived NPCs activate an early senescence
295 program that hampers physiological lineage commitment/differentiation. This senescent phenotype is
296 patient-specific (as it is not evident in GLD1 cells), and is rescued by supplying physiological levels of a
297 functional GALC enzyme.
298
299 **GLD cells display an altered lipidomic profile during the iPSC to neural differentiation**
300 Sphingolipids display widespread developmental, physiological and pathological actions in the
301 CNS, and induce biological effects on various stem/progenitor cell types (Hannun and Obeid, 2017). Given
302 the central role of GALC in the sphingolipid metabolism, we performed an untargeted global lipidomic
303 profiling in ND, GLD, and GLD^{GALC} iPSCs, NPCs and neuronal/glial cell progeny (d14 of differentiation) to
304 elucidate the impact of GALC absence or enhanced expression during the iPSCs to neural differentiation.
305 Lipid extracts were normalized based on protein concentration and analyzed by LC-MS-based lipidomics
306 workflow. We determined the lipid species showing reproducible changes in two independent profiling
307 experiments with two biological replicates for each experiment.
308 We identified more than 800 lipid species, with a distinct signature and enrichment of specific lipid
309 classes in iPSCs (e.g. triacylglycerols, TAG; lyso-phosphatidylserine, LPS), NPCs (e.g. phosphatidylcholine,
310 PC), and differentiated progeny (e.g phosphatidylethanolamine, PE; sphingomyelin, SM) (**Figure 7A**). We
311 observed profound changes in a number of phospholipid classes in GLD as compared to ND cells (i.e. TAG;
312 Diacylglycerols, DAG; Monoacylglycerols, MAG; PC; PE; Lysophosphatidylethanolamine, LPE; PS; SM;
313 Ceramides, Cer; HexosylCeramides, HexCer)(**Figure 7B**). Within the same lipid class, we detected

differences related to the stage of differentiation (iPSCs vs. NPCs. vs differentiated cells) and genotype (ND vs. GLD1 vs. GLD5). GLD1 and ND iPSCs often showed a comparable abundance of all these lipid classes, while GLD5 iPSCs displayed a clearly different trend (**Figure 7B**). The most striking differences between GLD1 and ND cells were observed in NPCs, which showed decreased levels of PE/LPE and increased Cer and DAG levels. The different lipidomic profile displayed by GLD1 and GLD5 cells become more evident as cells undergo differentiation. Indeed, when compared to GLD1 and ND cells, GLD5 cells showed reduced PC, PE, HexCer, and SM, and a strong accumulation of DAG, TAG, Cer, and PS **(Figure 7B**). The inverse pattern of Cer and SM expression in GLD5 cell populations - and particularly in differentiated cells - suggests that excess Cer could result from the SM-based synthetic pathway in these cells (Young et al., 2012).

LV-mediated rescue of GALC activity partially normalized the lipidomic profiles of GLD1 and GLD5, as shown by the PCA analysis (**Figure 7C)** and lipid signature **(Figure S9A-B).** In GLD1^{GALC} cells we observed a rescue of PC, PE, HexCer (iPSCs) and TAG (NPCs). In GLD5 ^{GALC} cells we observed the normalization of HexCer and SM level, as well as a rescue to normal levels of all DAG, TAG and PC that were mostly affected in GLD5 differentiated cells. LV-mediated GALC overexpression resulted in a profound and global impact on the lipidome of ND cells. Coherently with the presence of supranormal GALC activity, we detected in ND^{GALC} iPSCs, NPCs, and differentiated cells decreased levels of HexCer and variable increase of Cer, but also of DAG and PS, in comparison to ND counterparts (**Figure S9C**).

Discussion

Human iPSCs have been differentiated into neurons and/or glial cells to model the neural defects associated to several lysosomal storage diseases (LSDs) including mucopolysaccharidosis (Bayó-Puxan et al., 2018; Canals et al., 2015; Kobolák et al., 2019; Lemonnier et al., 2011; Vallejo-Diez et al., 2018), Niemann−Pick type C (Maetzel et al., 2014; Ordoñez and Steele, 2016; Trilck et al., 2013; Yu et al., 2014), Pompe disease (Higuchi et al., 2014), Gaucher disease (Panicker et al., 2012; Sun et al., 2015; Tiscornia et al., 2013), GM1 and GM2 gangliosidosis (Son et al., 2015)(Allende et al., 2018), NCL (Lojewski et al., 2014), and MLD (Frati et al., 2018; Meneghini et al., 2017). To our knowledge this is the first report describing a human iPSC-based neural model of GLD.

The five GLD patient-derived fibroblast cell lines that we used for somatic cell reprogramming have different mutations in the *GALC* gene, all of them associated to the infantile form of the disease. All the selected GLD iPSC lines displayed normal phenotypic and functional properties despite having undetectable GALC enzymatic activity and significant psychosine storage. The dispensability of lysosomal

enzymatic activity for somatic cell reprogramming and iPSC maintenance as well as the tolerability to lipid storage has been described in human iPSCs in other LSD models (Canals et al., 2015; Lojewski et al., 2014; Meneghini et al., 2017; Trilck et al., 2013). The LV-mediated supply of physiological or slightly supraphysiological GALC activity (3-4 fold the ND levels) in GLD iPSCs normalizes psychosine levels, confirming the potential of gene transfer to correct the primary storage in GALC-deficient human cells. In line with our previous study (Meneghini et al., 2017), we did not experience LV-mediated toxicity in hiPSCs, which were viable and functional for several passages after transduction, maintaining pluripotency and stable GALC activity.

The GALC enzyme contributes to preserve NPCs functionality during post-natal murine CNS development (Santambrogio et al., 2012), but this aspect was never investigated in human NPCs, neurons, and glial cells. GLD iPSC-derived NPCs had levels of psychosine similar to their ND counterparts, differently from the parental GLD fibroblasts and iPSCs, in which psychosine is elevated. Interestingly, the negligible psychosine storage in human NPCs distinguishes them from their murine counterpart (Santambrogio et al., 2012). The differentiation of GLD iPSC-NPCs into neurons and glia exacerbates psychosine accumulation and highlights a pathological phenotype, in line with the relevant role of GALC during CNS differentiation (Graziano and Cardile, 2015). Specifically, we observed an early and persistent loss of oligodendroglial cells in both GLD1 and GLD5 NPC-derived cultures. GLD5 (but not GLD1) cultures also displayed a dramatic loss of neurons. A modest psychosine storage may affect murine neuronal and glial differentiation from NPCs (Castelvetri et al., 2011; Santambrogio et al., 2012; Teixeira et al., 2014) before overt toxicity mediated by storage overload (Hawkins-Salsbury et al., 2013; White et al., 2011)(Bongarzone et al., 2016; Ricca and Gritti, 2016). Interestingly, psychosine storage has been detected in the brain of GLD human foetuses (Igisu and Suzuki, 1984) and elevated psychosine blood concentration is considered a specific marker in infantile GLD patients (Escolar et al., 2017), who may display early white matter changes and functional disability (Gupta et al., 2015). The aggravated defects in neuronal/glial differentiation from human NPCs described here are in line with these clinical observations. Also, several findings in this study suggest a composite and mutation-dependent effect associated to GALC deficiency which impacts on human NPC commitment/differentiation besides psychosine toxicity: i) psychosine accumulation starts at early time points of NPC differentiation and increases as cells differentiate into neurons and glia; still, this progressive load is not accompanied by a dramatic increase of apoptotic cells; ii) higher percentages of marker-negative cells are constantly found in GLD differentiated cultures, together with altered expression of key genes involved in oligodendroglial, neuronal, and astroglial specification/maintenance, suggesting a block in cell commitment or differentiation; iii) we observe only

a partial rescue of the differentiation program in LV.hGALC-transduced GLD neurons/glia - in which psychosine storage is cleared - with an evident amelioration in the neuronal compartment but far less improvement in the oligodendroglial population.

In the attempt of elucidating the link between GALC deficiency and defective neural differentiation, the mechanisms of disease correction upon gene transfer, and the mechanisms underlying the mutation-specific phenotype, we pointed our attention on the lipidome. Intriguingly, many sphingolipids involved in the GALC pathway, such as ceramide, sphingosine, and sphingosine-1-phosphate, contribute to proliferation, migration, cell fate, apoptosis (Hannun and Obeid, 2008, 2017), senescence and autophagy (Trayssac et al., 2018; Young and Wang, 2018). We previously documented the unbalance of some bioactive lipids in brain tissues of GLD mice (Santambrogio et al., 2012). Here, we show a distinctive global lipid profile in iPSCs vs. NPCs. vs. NPC progeny, regardless of the genotype (ND, GLD) or mutation (GLD1, GLD5), providing for the first time a snapshot of the changes in lipid metabolism during the iPSC to neural differentiation. By comparing the global lipidomic profile in each cell population, we observed that GLD and ND cells differ for the abundance of various fatty acids and phospolipid classes. The mild unbalance of lipid composition in GLD NPCs becomes more evident as cells differentiate. Intriguingly, GLD1 and GLD5 cell populations displayed remarkable differences in their lipidomic profile. Specifically, GLD5 iPSCs and NPC progeny show an accumulation of TAG, DAG, and ceramide, whose role in cell fate, cellular stress, ageing and replicative senescence has been proposed in multiple tissues and cell types (Hannun and Obeid, 2002, 2017; Lizardo et al., 2017, 2018; Venable et al., 1995). We envisage that this peculiar lipid perturbation contributes to the early senescence response and differentiation defects observed in GLD5 iPSC-derived neural cells. Considering that ceramide is the product of GalCer degradation by GALC, its accumulation in GLD5 lines is counterintuitive. We speculate that other major pathways leading to ceramide production may be induced in GLD5 cells, i.e. activation of sphingomyelinases and/or ceramide synthases (Claus et al., 2009; Mullen et al., 2012). The SM-ceramide pathway is particularly intriguing, since it may induce apoptosis, differentiation, and growth arrest (Jana et al., 2009). SM might be converted into ceramide via sphingomyelinase to compensate GALC deficiency. Moreover the parallel accumulation of DAG and TAG might be explained by an inhibition of the Kennedy pathway that is essential for *de novo* glycerophospholipid biosynthesis and the SM cycle in sphingolipid metabolism (Bieberich, 2012). Importantly, our data suggest that normalization of GALC activity rescues or at least ameliorates the global lipid composition of mutant cells.

The association between lysosomal dysfunction, lipid unbalance, and senescence in NPCs, neurons, and glial cells and its contribution to neurodegeneration and demyelination is emerging as an

area of active scientific investigations. Specifically, by taking advantage of mouse models or post-mortem human brain samples it was reported that senescence functionally contributes to multiple sclerosis pathogenesis (Nicaise et al., 2019) as well as to cognitive defects in Alzheimer disease (Zhang et al., 2019). Notably, our study highlights the importance of performing this investigation in relevant human iPSC-based neural models, which recapitulate the patient-specific pathological hallmarks more faithfully as compared to murine models or non-neural cells.

Our study raises a number of relevant mechanistic questions. First, the respective role and potential interaction between psychosine load and lipidome perturbation in determining the different phenotype in GLD5 vs. GLD1 are not fully elucidated. One option would be the detrimental action exerted by psychosine and ceramide (and possibly other lipid classes, e.g. TAG) preferentially on oligodendrocyte and neuronal cells, respectively (Jana et al., 2009). Second, while our results suggest an association between ceramide/TAG/DAG accumulation and senescence, the mechanistic link between the GLD5 mutation and the occurrence of this specific lipid unbalance is not clear yet. Possibilities include: i) a direct effect of the mutated GALC protein on the lipidome (the investigation of the lipid-protein interactions and definition of the molecular mechanisms of pathway and enzyme regulation are rapidly expanding in the field of bioactive lipids) (Hannun and Obeid, 2017); ii) an indirect effect of another GLD-associated pathology (i.e. oxidative stress, mitochondrial dysfunction) (Ricca and Gritti, 2016)(Ballabio and Gieselmann, 2009). The use of isogenic pairs might clarify whether the GLD5 mutated protein has a dominant negative effect that contribute to the pathogenic phenotype in addition to the enzymatic deficiency.

In summary, our data show that GALC deficiency severely affects the differentiation of hiPSC-derived neural progenitors into neurons and oligodendrocytes. We highlight cell type-, and patient-specific disease hallmarks in GLD cells, including galactosylsphingolipid storage, lipidome perturbation, and activation of a senescence program. Finally, we show that a timely regulated GALC expression is critical for proper neural commitment and differentiation. We anticipate these findings to be starting point for future functional experiments aimed at further dissecting the complex and mutation-specific GLD pathology. This knowledge will pave the way to tailored gene/cell therapy strategies to enhance the correction of CNS pathology in GLD.

Acknowledgments

440 We are grateful to Lucia Sergi Sergi for LV preparation and titration, Andrea Ditadi for providing the ESC
441 line H9, Wim Kulik for psychosine analyses, Janet Elizabeth Deane for providing the anti-hGALC antibody,
442 all the members of the Gritti's lab for generous support and helpful discussion.
443 Part of this work was carried out in ALEMBIC, an advanced microscopy laboratory established by IRCCS
444 Ospedale San Raffaele and Università Vita-Salute San Raffaele.
445 We thank the "Diagnosi PrePostnatale Malattie Metaboliche" Laboratory (G.Gaslini Institute) for providing
446 us with specimens from the "Cell line and DNA bank from patients affected by Genetic diseases" Biobank
447 - Telethon Genetic Biobank Network (project no. GTB07001A).
448
449 This study was funded by grants from Fondazione Telethon (Tiget Core Grant 2016-2021, project D2) and
450 European Leukodystrophy Association (grant ELA 2016-010I3) to A.G.
451 R.D.M was supported by Fondazione Telethon (Tiget Core Grant 2016-2021, grant E5), a Career
452 Development Award from Human Frontier Science Program (HFSP), an Advanced Research Grant from the
453 European Hematology Association (EHA), "Pilot and Seed Grant 2015" from the San Raffaele Hospital, a
454 Hollis Brownstein Research Grant from Leukemia Research Foundation (LRF), the Interstellar Initiative on
455 Healthy Longevity from NYAS and AMED and by AIRC (MFAG 2019 - ID. 23321 project).
456 D.G was supported by the IBSA Foundation postdoctoral fellowship.
457 E.M was supported by a FCSR (Fondazione Centro San Raffaele) postdoctoral fellowship.
458 E.M., A.Ce., and L.d.V. conducted this study as partial fulfillment of their international Ph.D. in Molecular
459 Medicine, Vita-Salute San Raffaele University.
460

461 **Author contribution**

462 Conceptualization, A.G. and E.M.
463 Methodology, E.M, A.B, R.dM, S.M
464 Investigation, E.M., A.Ce, A.Ca., F.M., D.G., L.d.V., V.M., F.S., M.P, L.S.
465 Writing –Review & Editing, A.G., E.M, R.dM., A.B
466 Funding Acquisition, A.G.
467 Resources, S.M., A.B., R.dM., F.S.
468 Supervision, A.G., R.dM., A.B.
469

470 **Declaration of interests**

471 The authors declare no competing interests.

472

473 **Figures and legends**

Figure 1

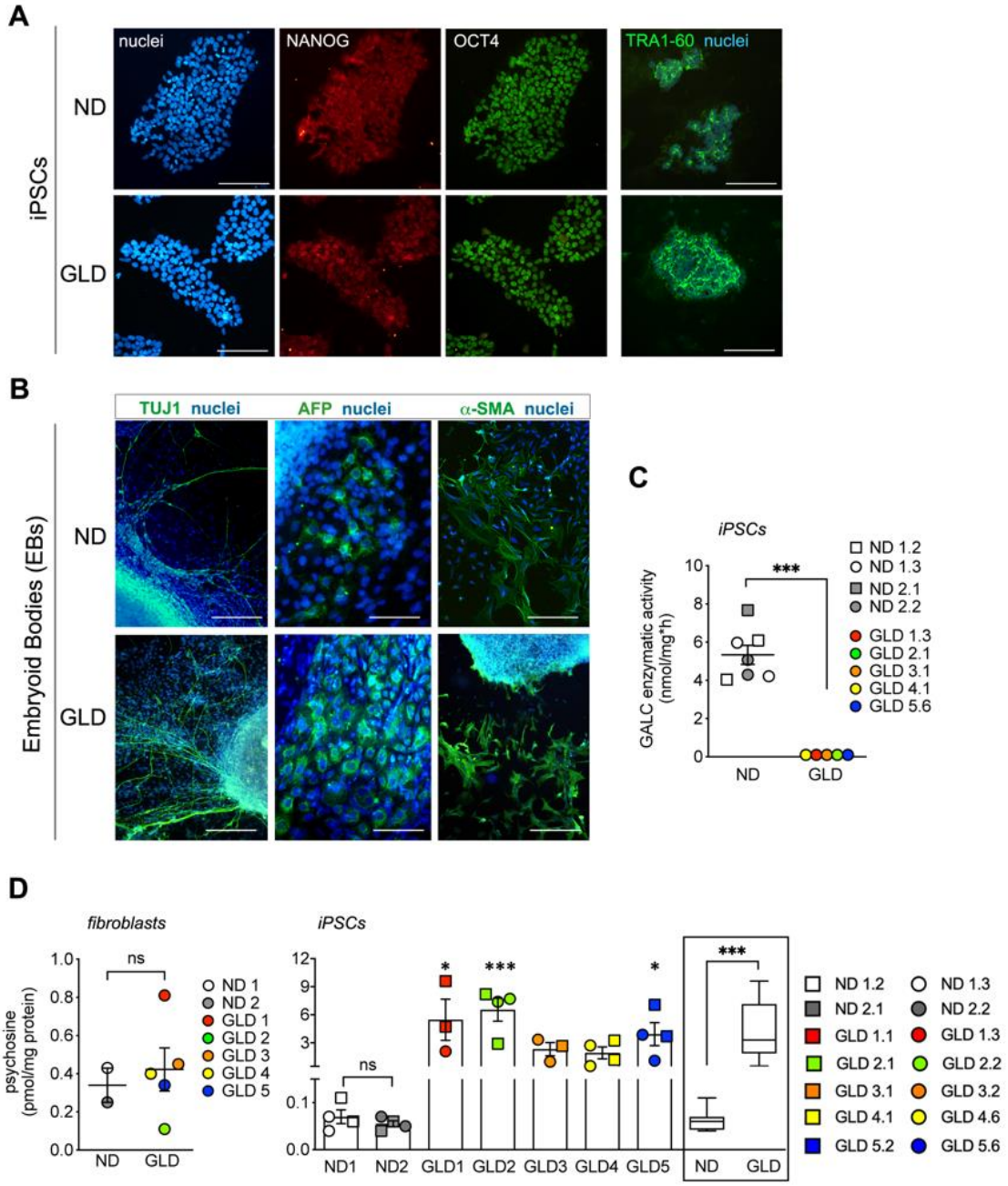

474

475 **Figure 1. GLD iPSCs have undetectable GALC activity and increased psychosine levels (see also Figures S1 and S2)**

476 A) Representative confocal immunofluorescence pictures of ND and GLD iPSCs expressing OCT4 (green), NANOG

477 (red), and TRA 1-60 (green). Nuclei are counterstained with Hoechst (blue). Single channels (OCT4, NANOG, nuclei)

478 and the merged picture (TRA 1-60/nuclei) are shown. Scale bars: 100μm.

B) Representative immunofluorescence pictures showing cells expressing endodermal (AFP), mesodermal (α-SMA), and ectodermal (TUJ1) markers in ND and GLD embryoid bodies (EBs). Lineage markers in green, nuclei counterstained with Hoechst (blue). Scale bars: 80 µm (AFP) and 200 µm (TUJ1 and α-SMA).

C) GALC enzymatic activity in ND and GLD iPSC clones. Data are expressed as the mean ± SEM and analyzed using Mann-Whitney test; ***$p<0.001$.

D) Psychosine levels measured by mass spectrometry in ND1 (white circles), ND2 (grey circles), and GLD (colored circles) fibroblast cell lines (n=1 sample/line) and the corresponding iPSC clones (n=2 clones/line in single or duplicate). Data are expressed as the mean ± SEM and analyzed by Mann-Whitney test (fibroblasts) and Kruskal Wallis test followed by Dunns' multiple comparison test (iPSCs); ns, not significant * $p<0.05$, ***$p<0.001$ vs ND (mean). The mean ± SEM of all ND and GLD clones are plotted in the box and whiskers graph and analyzed by Mann-Whitney test; ***$p<0.001$.

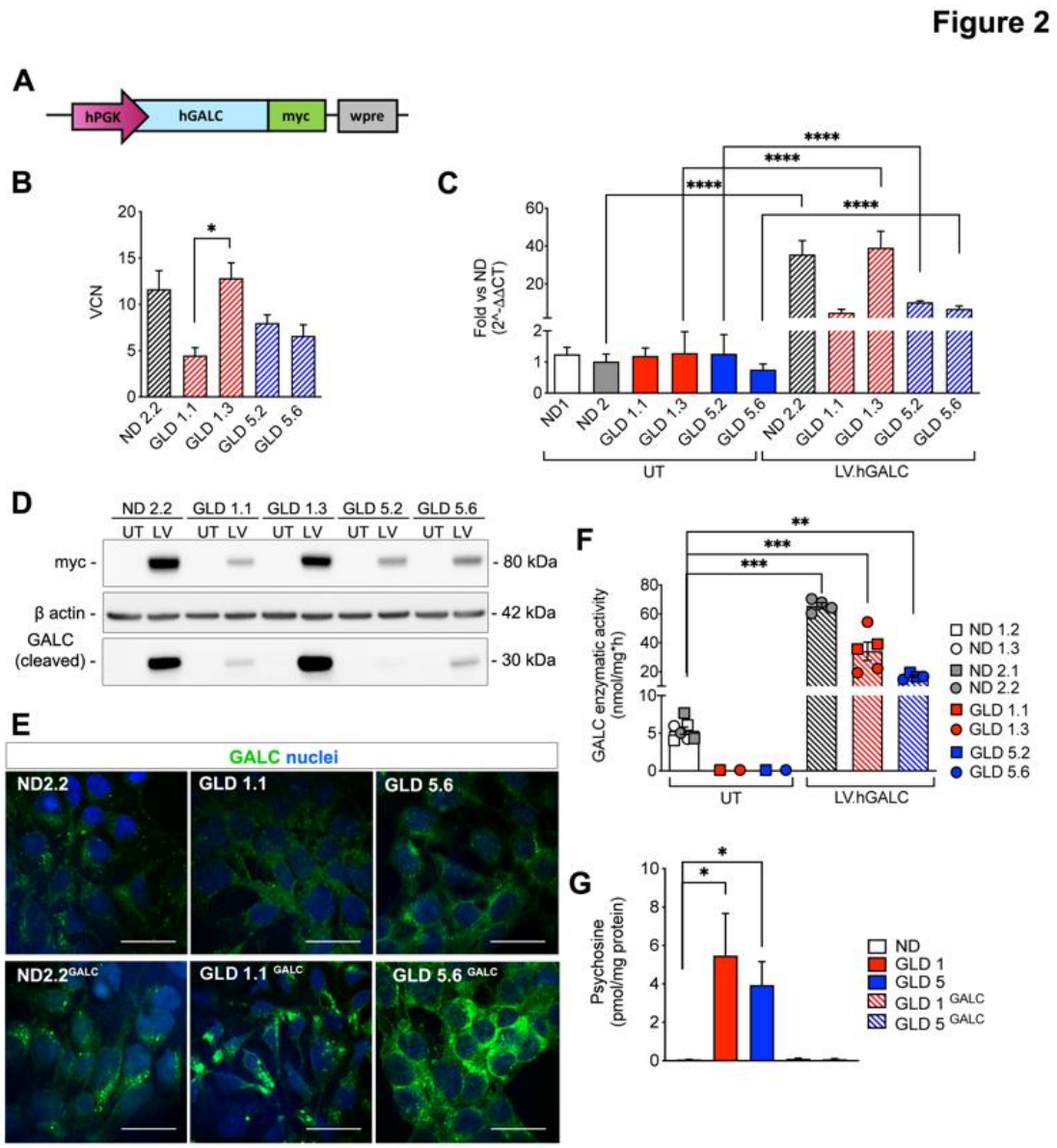

Figure 2. LV-mediated gene transfer rescues GALC expression and enzymatic activity in GLD iPSCs (see also Figure S3)

A) Schematic representation of the LV.hGALC vector. hPGK, human phosphoglycerate kinase promoter; wpre, Woodchuck hepatitis virus Post-transcriptional Regulatory Element.

B) Vector Copy Number measured in ND and GLD iPSCs clones transduced with LV.hGALC at multiplicity of infection= 2 (MOI2). Data are expressed as the mean ± SEM (n=2-4 replicates/clone) and analyzed using Kruskal Wallis test followed by Dunnett's multiple comparison post-test; *p<0.05.

C) GALC mRNA expression in untreated (UT; solid bars) and LV.hGALC-transduced (striped bars). n=3 replicates/clone. Values are normalized on GAPDH and expressed as fold change (2^-ΔΔCT) vs ND (mean). Data are expressed as mean ± SEM and analysed using one-way Anova followed by Turkey multiple comparison post-test; **** p<0.0001.

D) Representative Western Blot showing the expression of the GALC-myc fusion protein using an anti-myc antibody (band size 80 kDa, precursor protein and an anti-hGALC antibody (band size 30 kDa, cleaved protein) in LV.hGALC transduced (LV; MOI2) ND and GLD iPSCs clones. β-actin was used as loading control. Note that higher protein expression in clones ND2.2 and GLD 1.3, which show higher VCN (B) and GALC activity (C, F). Untransduced (UT) clones do not express the myc-tagged protein (80kDa). The 30KDa band is undetectable in UT clones due to the low levels of physiological protein expression (see also panel E).

E) Representative immunofluorescence pictures showing the expression of the GALC protein (green; anti-hGALC) in untransduced (UT) and LV.hGALC transduced ND and GLD iPSCs. Nuclei are counterstained with Hoechst (blue). Scale bars= 20μm.

F-G) GALC enzymatic activity (F) and Psychosine levels (G; clones as in F) in untransduced (UT, solid bars) and LV.hGALC transduced (striped bars) ND, GLD and iPSCs. Data are expressed as the mean ± SEM (n=2-4 replicates/clone). Data were analyzed by Kruskal Wallis test followed by Dunnett's multiple comparison post-test (ND selected as control group); **$p < 0.01$; ***$p < 0.001$; ns, not significant.

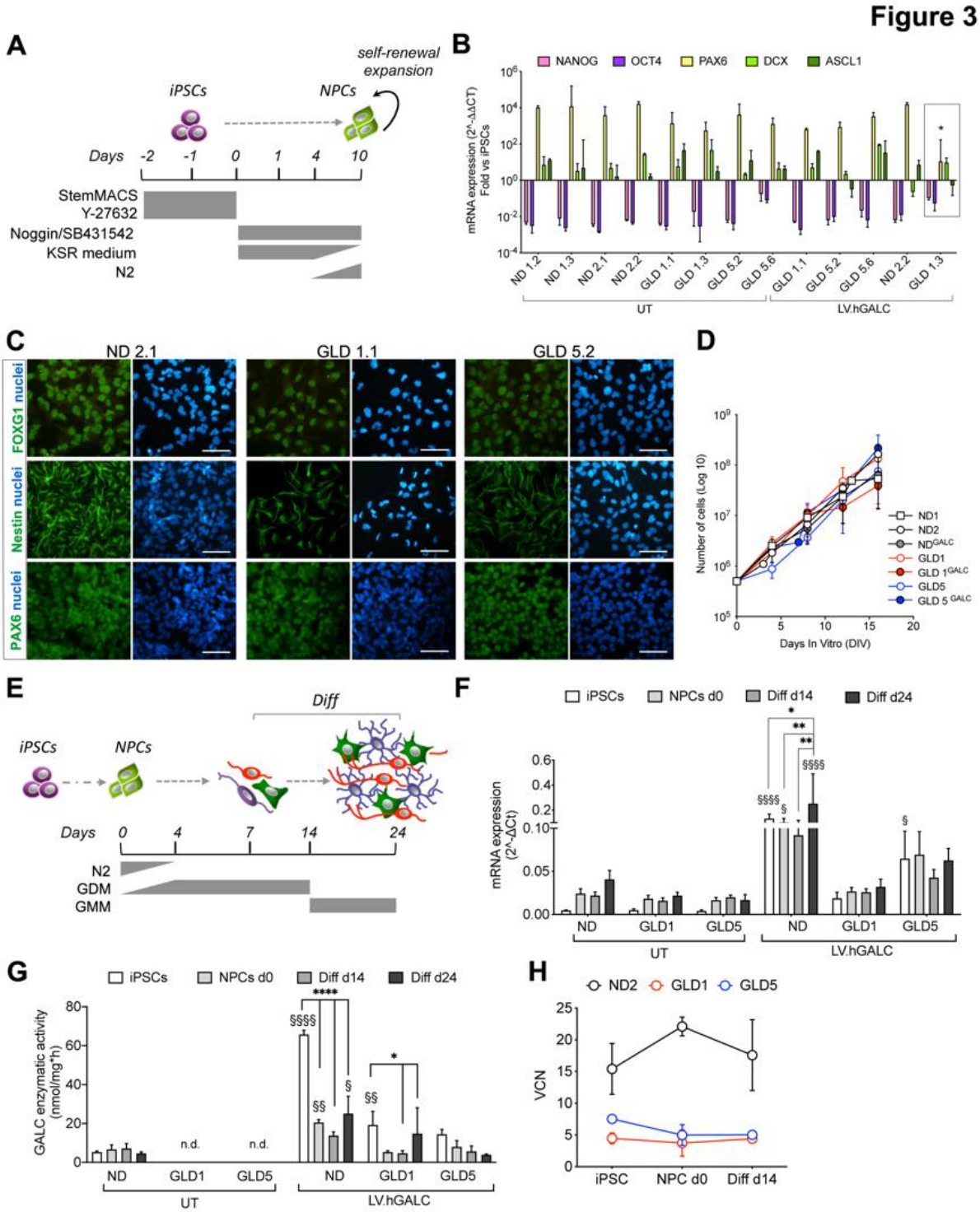

Figure 3. Differentiation of ND and GLD iPSCs into NPCs, neurons and glial cells

A) Schematic representation of the protocol used to differentiate iPSCs into NPCs.

B) Downregulation of the expression of pluripotency-associated markers (NANOG, OCT4) and upregulation of the expression of NPC markers (PAX6, DCX, ASCL1) in untransduced (UT) and LV.hGALC-transduced ND and GLD iPSC-derived NPC populations (assessed by SYBR green RT-PCR). Data are normalized on GAPDH expression and shown as

fold change (2^-ΔΔCT) on the corresponding iPSC clone. Data are expressed as the mean ± SEM (n=3-4 independent experiments; 2-3 replicates/clone). The GLD1.3 clone (box) showed reduced upregulation of PAX6. Data analyzed using Kruskal Wallis test followed by Dunnett's multiple comparison post-test (ND selected as control group). *p<0.05.

C) Representative immunofluorescence pictures showing the expression of the neural markers Nestin, FOXG1 and PAX6 (green) in ND and GLD iPSC-NPC cultures. Nuclei are counterstained with DAPI (blue). Scale bars=50μm.

D) Proliferation and stable expansion rate of untransduced and LV.hGALC transduced ND and GLD iPSC-NPC lines (subculturing passages 0 to 5 shown in the graph; 16 days in vitro, DIV). Each point of the curves is the mean ± SEM; n=2–3 independent experiments, 1-2 clones/group. Clones used: ND1.2, ND1.3, ND2.1, ND2.2, GLD1.1, GLD1.3, GLD5.2, GLD5.6.

E) Schematic representation of the differentiation protocol used to differentiate iPSC-NPCs (d0) into mixed neuronal/glial cultures that were analyzed in at day 7 (d7), d14, and d24. GDM, Glial Differentiation Medium; GMM, Glial Maturation Medium (see methods).

F) GALC mRNA expression in untransduced (UT) and LV.hGALC-transduced iPSCs and neural progeny (NPCs, d0; differentiated cells, d14 and d24) n.d.: not detectable. Values are normalized on GAPDH and expressed as (2^-ΔCT). Clones used: ND1.2, ND1.3, ND2.1, ND2.2, GLD1.1, GLD1.3, GLD5.2, GLD5.6

Data are expressed as the mean ± SEM (n=2-3 independent experiments; 1-2 replicates/clone). Data analyzed using two-way ANOVA. To compare the different time points (iPSC, NPC d0, differentiated cells, d14 and d24) in each group we used Turkey's multiple comparison post-test (*p < 0.05, **p < 0.01, ****p < 0.0001); to compare the different groups at each time point we used Dunnett's multiple comparison post-test (ND selected as control group). §p < 0.05, §§p < 0.01, §§§§p < 0.0001.

G) GALC enzymatic activity in untransduced (UT) and LV.hGALC-transduced ND and GLD iPSCs and neural progeny (NPCs, d0; differentiated cells, d14 and d24). Data are expressed as the mean ± SEM (n=2-4 replicates/clone). Data were analyzed by Kruskal Wallis test followed by Dunnett's multiple comparison post-test (ND selected as control group); *p < 0.01; ****p < 0.0001; ns, not significant.

H) Vector copy number (VCN) measured in LV.hGALC-transduced iPSCs and neural progeny (NPCs, d0; differentiated cells, d14). Clones used: ND2.2^{GALC}, GLD1.1^{GALC}, GLD5.2^{GALC}, GLD5.6^{GALC}; n= 1-3 independent experiments, 1-2 clones/group.

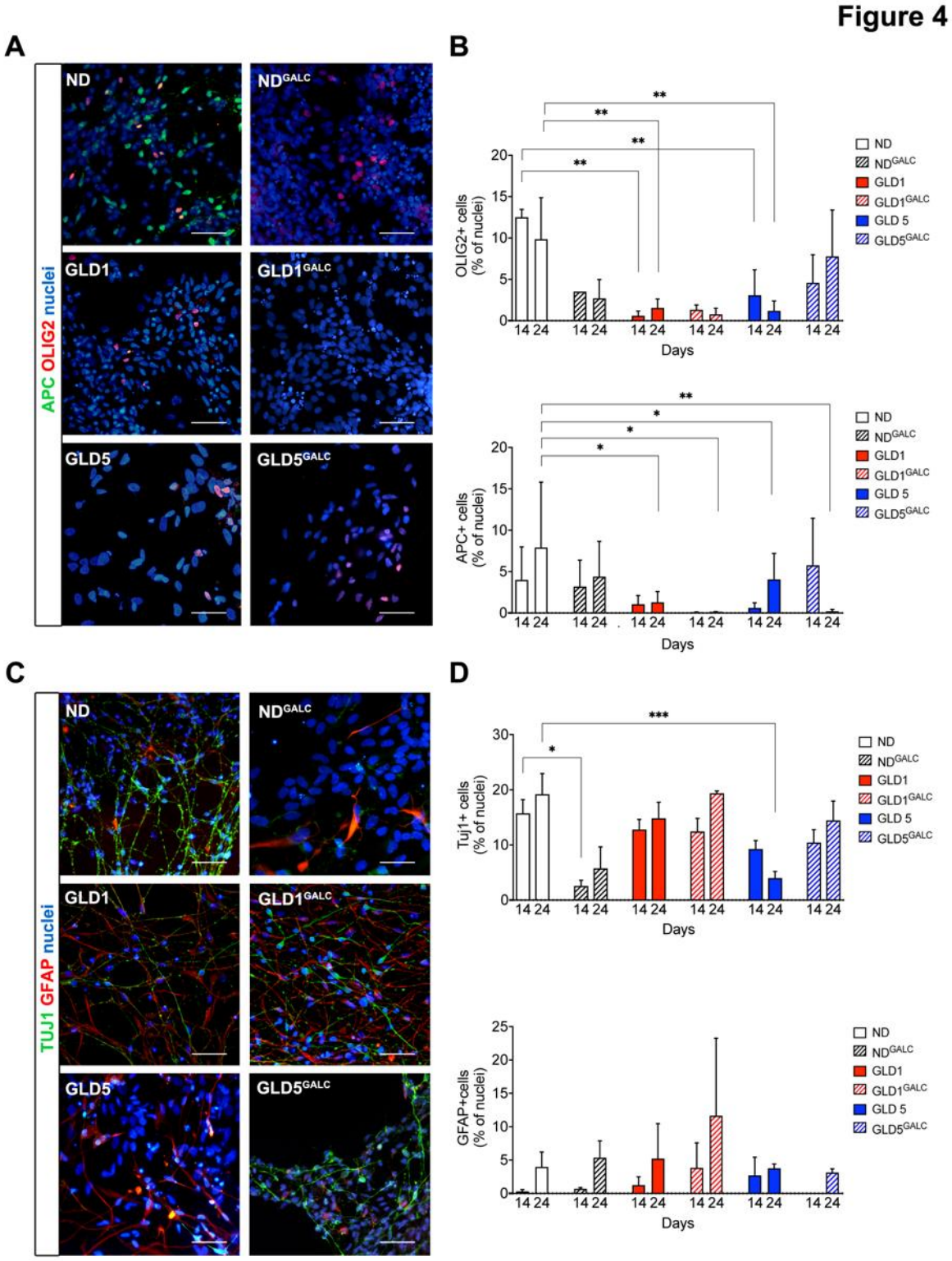

Figure 4. GLD NPCs display impaired neuronal and glial differentiation (see also Figures S4, S5, S6, S7)

A) Representative pictures of untransduced (UT) and LV.hGALC-transduced ND and GLD differentiated neural progeny (d24 of differentiation) expressing Olig2 (red) and APC (green). Nuclei are counterstained with Hoechst

(blue). Scale bar, 50 µm.

B) Quantification of cells expressing Olig2 and APC in UT and LV.hGALC-transduced ND and GLD differentiated neural progeny (d14 and d24).

C) Representative pictures of UT and LV.hGALC-transduced ND and GLD differentiated neural progeny (d24 of differentiation) expressing TUJ1 (green; neurons) and GFAP (red; astrocytes). Nuclei are counterstained with Hoechst (blue). Scale bar, 50 µm.

D) Quantification of cells expressing TUJ1 and GFAP in UT and LV.hGALC-transduced ND and GLD differentiated neural progeny (d14 and d24).

Data in B and D are expressed as percentage of immunoreactive (IR) cells on total nuclei and represent the mean+SEM; n= 2-4 independent experiments; 1-3 clones/group with 2–3 replicates/clone for each time point; 5-10 fields/coverslips were analyzed. Clones used: ND1.2, ND2.1, ND2.2, GLD1.1, GLD1.3, GLD5.2, GLD5.6, ND2.2^{GALC}, GLD1.1^{GALC}, GLD5.2^{GALC}, GLD5.6^{GALC}. Data were analyzed by two-way ANOVA followed by Dunnett's multiple comparison post-test (ND at the corresponding time point selected as control group). *$p<0.05$, **$p<0.01$, *** $p < 0.001$.

Figure 5

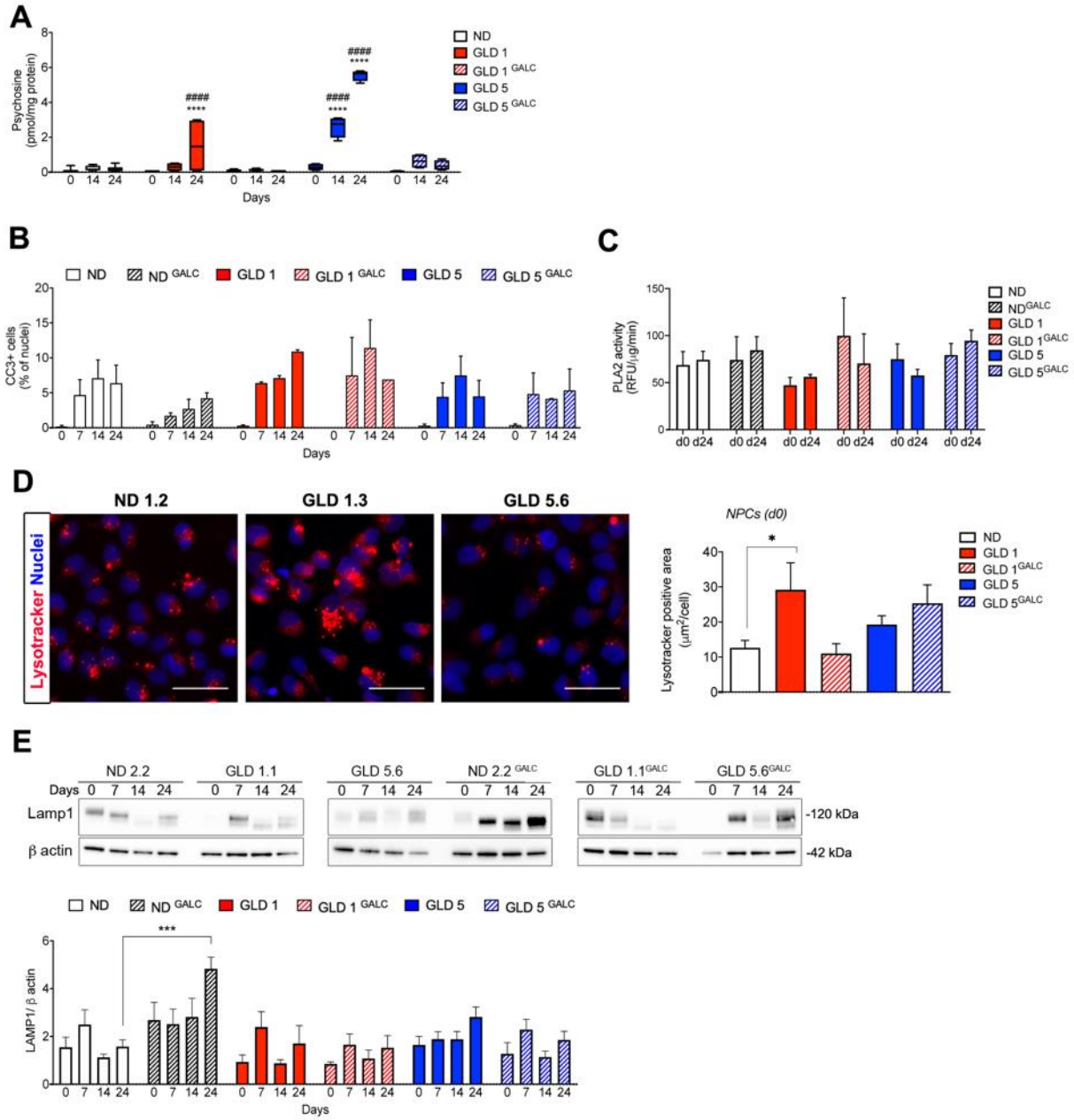

Figure 5. Pathological hallmarks in GLD neural progeny

A) Psychosine levels in UT and LV.hGALC-transduced ND and GLD NPCs (d0) and differentiated progeny (d14 and d24). Data are expressed as mean+SEM, n=2-4 replicates/clone, 1-3 clones/group. Clones used: ND1.2, ND2.1, ND2.2, GLD1.1, GLD1.3, GLD5.2, GLD5.6, ND2.2^{GALC}, GLD1.1^{GALC}, GLD5.2^{GALC}, GLD5.6^{GALC}. Data were analyzed by two-way ANOVA followed by Turkey's multiple comparison post-test; ****p<0.0001 GLD vs ND at the corresponding time point; $^{\#\#\#\#}$ p<0.0001 GLD vs GLD^{GALC} at the corresponding time point. p>0.05 GLD^{GALC} vs ND at all time points.

B) Quantification of cells expressing cleaved caspase 3 (CC3) in UT and LV.hGALC-transduced ND and GLD NPCs (d0)

578 and differentiated progeny (d14 and d24). Data are expressed as percentage of immunoreactive (IR) cells on total
579 nuclei and represent the mean+SEM; n= 2 independent experiments; 1-3 clones/group, 2–3 replicates/clone for each
580 time point; 5-10 fields/coverslips were analyzed. Clones used: ND1.2, ND2.1, ND2.2, GLD1.1, GLD1.3, GLD5.2, GLD5.6,
581 ND2.2^{GALC}, GLD1.1^{GALC}, GLD5.2^{GALC}, GLD5.6^{GALC}. Data were analyzed by two-way ANOVA followed by Dunnett's
582 multiple comparison post-test (ND at the corresponding time point selected as control group). No differences
583 between groups (p>0.05).
584 C) PLA2 activity in untransduced and LV.hGALC-transduced ND and GLD NPCs (d0) and differentiated progeny (d24).
585 Data are expressed as mean+SEM. n=2 independent experiments; 1-3 clones/group. Clones used: ND1.2, ND2.1,
586 ND2.2, GLD1.1, GLD1.3, GLD5.2, GLD5.6, ND2.2^{GALC}, GLD1.1^{GALC}, GLD5.2^{GALC}, GLD5.6^{GALC}.
587 D) Representative pictures of lysotracker-positive NPCs (red) and quantification of lysotracker-positive area
588 (μm^2/cell) in ND1.2, GLD1.3 and GLD5.6 clones. Nuclei are counterstained with Hoechst. Scale bars= 20μm. Data are
589 expressed as the mean+SEM, n=2 independent experiments, 3 wells/clone, 1.400-12.000 cells/well were analyzed.
590 Data analysed by two-way ANOVA followed by Dunnett's multiple comparison post-test (ND selected as control
591 group). *p<0,05.
592 E) Representative Western Blot and densitometric quantification showing the expression of the LAMP1 protein in UT
593 and LV.hGALC-transduced ND and GLD NPCs (d0) and differentiated progeny (d7, d14 and d24). β-actin was used as
594 loading control. Data are represented as the mean+SEM; n= 3-5 independent experiments; 1-4 clones/group. Data
595 were analyzed by two-way ANOVA followed by Dunnett's multiple comparison post-test (ND at the corresponding
596 time point selected as control group). * p<0.05, **p< 0.01; *** p < 0.001.
597

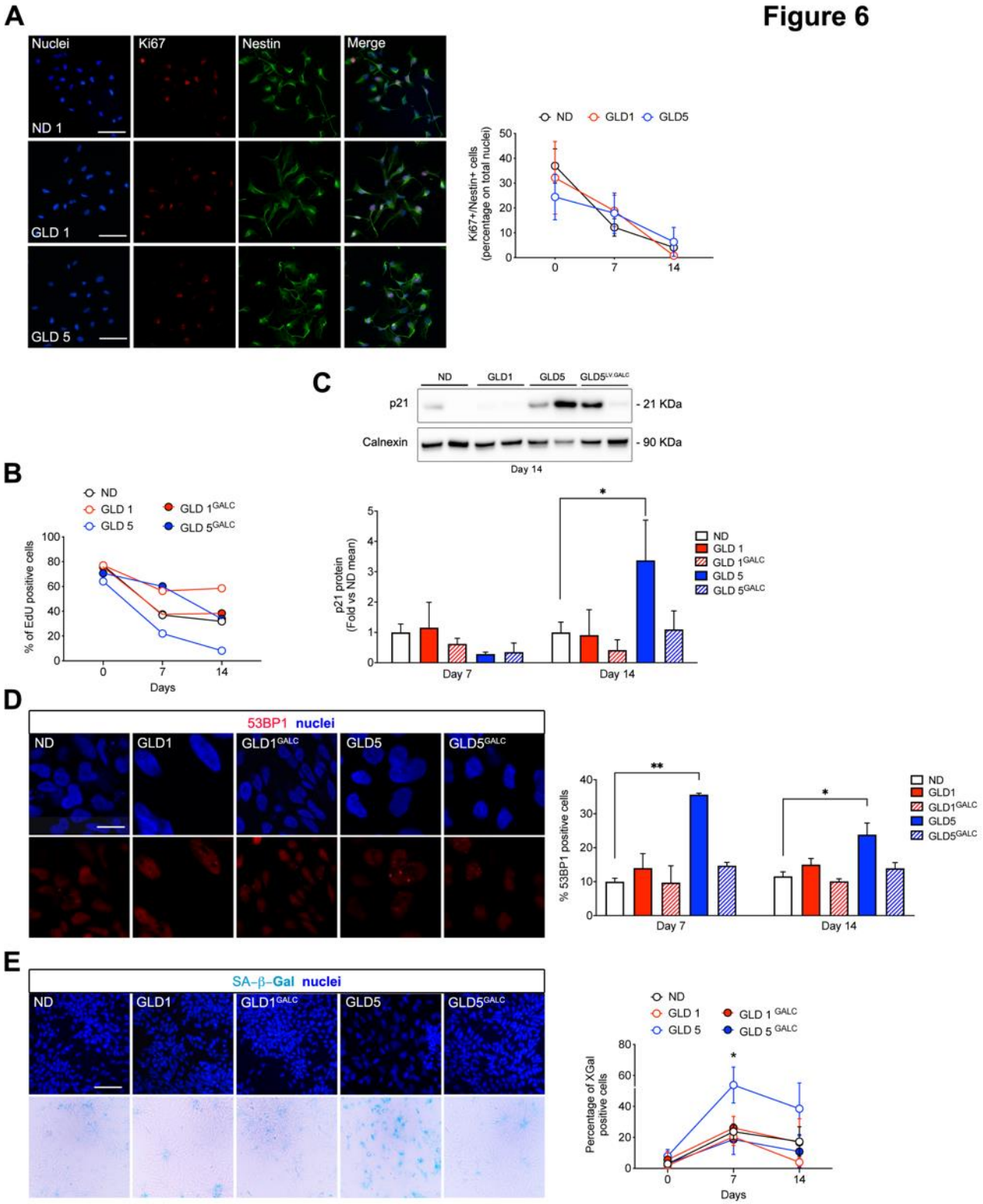

Figure 6. GLD5 NPCs progeny display markers of senescence (see also Figure S8)

A) Representative confocal immunofluorescence pictures and quantification of cells expressing nestin (green) and Ki67 (red) in ND, GLD, and GLD^{GALC} NPCs (d0; shown in the pictures) and differentiated cultures (d7 and d14). Nuclei

are counterstained with Hoechst. Scale bars= 50μm. Data in the graph are expressed as the mean+SEM n= 3 independent experiments; 1-3 clones/group with 1–3 replicates/clone for each time point; 5-10 fields/coverslips were analyzed. Clones used: ND1.2, ND1.3, ND2.1, ND2.2, GLD1.1, GLD1.3, GLD5.2, GLD5.6).

B) Quantification of EdU positive cells (after a 16 hour-pulse) in ND, GLD, and GLD^{GALC} NPCs (d0) and differentiated cultures (d7 and d14). Data in the graph are expressed as percentage over total cells (mean); n= 2 independent experiments for each time point, 1-2 clones/group. Clones used: ND1.2, ND2.2, GLD1.1, GLD5.2, GLD5.6, GLD1.1^{GALC}, GLD5.2^{GALC}.

C) Representative Western blot and densitometric quantification showing the expression of the p21 protein in ND, GLD, and GLD^{GALC} NPC differentiated progeny (d7 and d14; d14 shown in the blot). Calnexin was used as loading control. Data are expressed as fold vs ND at the corresponding time point (mean of all clones) and represented as the mean+SEM; n= 2 independent experiments; 1-3 clones/group. Clones used: ND1.2, ND2.2, GLD1.1, GLD1.3, GLD5.2, GLD5.6, GLD1.1^{GALC}, GLD5.2^{GALC}, GLD5.6^{GALC}. Data were analyzed by two-way ANOVA followed by Dunnett's multiple comparison post-test (ND at the corresponding time point selected as control group). * $p<0.05$.

D) Representative confocal immunofluorescence pictures and quantification for 53BP1-positive DDR foci in ND, GLD, and GLD^{GALC} NPC (d0) and differentiated cultures (d7 and d14; d14 shown in the pictures). Nuclei are counterstained with DAPI. Scale Bar = 15 μm (for all panels, shown in ND).

Clones used: ND1.2, ND2.2, GLD1.1, GLD1.3, GLD5.2, GLD5.6, GLD1.1^{GALC}, GLD5.2^{GALC}, GLD5.6^{GALC}. Data in the graph are expressed as the mean+SEM; n= 3 independent experiments, 2-3 replicates/clone for each time point. 100 to 600 nuclei per condition were analyzed. Data were analyzed by Kruskal Wallis test followed by Dunns' multiple comparison post-test (ND at the corresponding time point selected as control group). * $p<0.05$, ** $p < 0.01$.

E) Representative pictures (brightfield and immunofluorescence for nuclei) and quantification of SA-βGal-positive cells in ND, GLD, and GLD^{GALC} NPCs (d0) and differentiated cultures (d7 and d14; d7 shown in the pictures). Nuclei are counterstained with Hoechst. Scale bars= 50μm (for all panels, shown in ND). Data in the graph are expressed as the mean+SEM n= 3 independent experiments; 1-3 clones/group, 1–3 replicates/clone for each time point; 4-10 fields/coverslips were analyzed. Clones used: ND1.2, ND2.1, ND2.2, GLD1.1, GLD5.2, GLD5.6, GLD1.1^{GALC}, GLD5.2^{GALC}, GLD5.6^{GALC}. Data were analyzed by two-way ANOVA followed by Dunnett's multiple comparison post-test (ND at the corresponding time point selected as control group). * $p<0.05$.

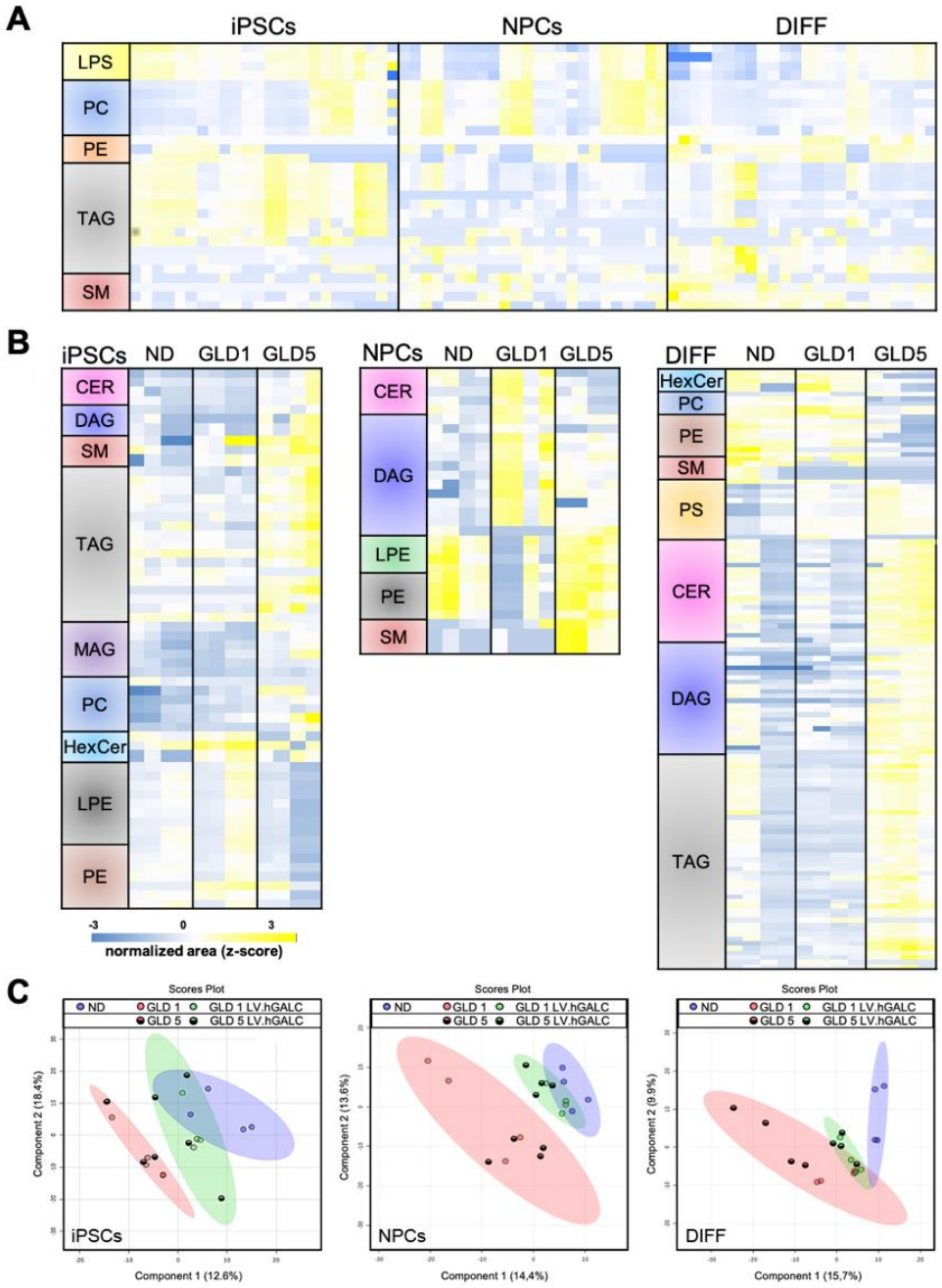

Figure 7. Lipidomic profile during iPSC neural differentiation (see also Figure S9)

A) Hierarchical clustering of lipid species differently enriched in iPSCs, NPCs and differentiated cultures (d14). ANOVA statistical test was applied (FDR<0.05).

B) Hierarchical clustering of lipid species differently enriched in ND, GLD1 and GLD5 iPSCs, NPCs and differentiated cultures (d14). ANOVA statistical test was applied (FDR<0.05).

C) Principal component analysis (PCA) of lipid species distribution in ND, GLD and LV.hGALC transduced GLD iPSCs, NPCs and differentiated cultures (d14 of differentiation). Clones used: ND2.2, GLD1.1, GLD5.2, ND2.2^{GALC}, GLD1.1^{GALC}, GLD5.2^{GALC}. See methods for abbreviation of lipid classes.

Methods

Reagents generated in this study are available upon request from the Lead Contact with a completed Materials Transfer Agreement.

The lipidomic dataset generated during this study is uploaded at MetaboLights, weblink https://www.ebi.ac.uk/metabolights/MTBLS1501. The public release date is set to Feb 15 00:00:00 GMT 2021.

Generation of iPSCs from human fibroblasts.

Human dermal fibroblasts from healthy donors (ND1 and ND2) were purchased from Life technologies. Fibroblasts from GLD patients (GLD1, GLD2, GLD3, GLD4, and GLD5) and of a non-affected relative of GLD1 (ND3) were obtained from the Cell Line and DNA Bank of Patients affected by Genetic Diseases (Gaslini Institute, Genova, Italy). Human fibroblasts were cultured in Dulbecco's modified Eagle's medium (DMEM) supplemented with 10% fetal bovine serum (FBS), L-glutamine, and penicillin/streptomycin in an humidified atmosphere, 5% CO_2 at 37°C. Fibroblasts at passages (p) 4-5 (GLD1, GLD2, GLD3, ND1, ND2) and p10-11 (GLD4 and GLD5, ND3) were used for reprogramming.

Reprogramming was outsourced to BioERA (Padova, Italy). Reprogramming factors were delivered as modified mRNAs (mmRNAs) taking advantage of a microfluidic system (Luni et al., 2016). The StemMACS mRNA Reprogramming Kit (Miltenyi Biotec, Bergisch Gladbach, Germany) was used for mRNA transfection according to the manufacturer instructions. Colonies positive for NANOG and TRA-1-60 were catalogued as iPSCs with progressive numbering. Six randomly selected colonies/donor were picked and expanded for 2 passages. Cells were then frozen; two frozen vials/donor were sent to SR-Tiget. The iPSCs obtained from BioERA were thawed and cultured on matrigel-coated (BD Biosciences, Erembodegen, Belgium) plastic dishes in StemMACS™ iPS-Brew XF medium (Miltenyi Biotech) in an humidified atmosphere, 5% O_2, 5% CO_2 at 37°C. The medium was changed daily. For routine passage, cells were detached in PBS containing 0,5 mM EDTA and split at 1:3 to 1:10 ratio. Accutase (Sigma-Aldrich, Saint Louis, USA) was used for single cell dissociation of iPSC colonies.

Human cells were used according to the guidelines on human research issued by the San Raffaele Scientific Institute's ethics committee (protocol TIGET-HPCT).

Karyotype analysis.

Karyotyping was performed as previously described (Meneghini et al., 2017). Briefly, iPSC cultures were treated with KaryoMAX colcemid 0,1 mg/ml (Life Technologies, Carlsbad, USA) for 2 h at 37°C. After

671 hypotonic treatment with 0,075 M KCl and fixation in methanol: acetic acid (3:1), the cell suspension was
672 dropped onto a microscopy slide and air-dried. Chromosome counts and G-banding karyotype analyses
673 were done on metaphases stained with Vectashield mounting medium with DAPI (Vector Laboratories,
674 Burlingame, USA). Images were analysed with Applied Imaging Software CytoVision (CytoVision Master
675 System). We counted >10 metaphases/coverslip. The karyotype is considered normal when >90% of the
676 counted metaphases are normal (46, XX or 46, XY).
677
678 **Embryoid Bodies formation.**
679 iPSC colonies were gently detached using a scraper, dissociated in small cell clumps using a 2ml pipette,
680 plated in Ultra-low attachment plates (Corning, New York, USA) and grown in suspension for 10 days in EB
681 medium: DMEM-F12+20% Knockout Serum Replacement (KSR), non-essential aminoacids, Sodium
682 Piruvate, L-glutamine, penicillin/streptomycin and 0,1 mM β-mercaptoethanol. The resulting spheroids
683 were allowed to reattach on matrigel-coated 6-well plates or glass coverslips to continue differentiation
684 for additional 10 days. Finally, they were collected for RNA extraction or fixed with 4% paraformaldehyde
685 (PFA) for immunofluorescence analyses.
686
687 **iPSCs differentiation into NPCs**.
688 For neural induction of iPSCs we applied a dual-smad inhibition protocol (Chambers et al., 2009, 2011).
689 Briefly, iPSC colonies were detached using Accutase, suspended as single cells and plated on Matrigel-
690 coated dishes (75,000 cells/cm^2) in StemMACS™ iPS-Brew XF medium supplemented with 10 µM of ROCK
691 inhibitor Y-27632 (Sigma-Aldrich). At ≈90% confluence (usually 2 days after plating), culture medium was
692 replaced with KSR medium (Chambers et al., 2009, 2011) supplemented with 200 ng/ml of recombinant
693 human Noggin (R&D Systems, Minneapolis, USA) and 10 µM of SB431542 (Sigma-Aldrich). The medium
694 was changed daily for the next 3 days. At day 4, KSR medium was gradually switched to N2 medium
695 (Chambers et al., 2009, 2011) containing Noggin and SB431542 (75-25%, 50-50%, 25-75% every two days).
696 After 10 days, cells were detached using Accutase and plated on Matrigel-coated dishes in N2 medium
697 supplemented with 20 ng/ml bFGF, 20 ng/ml EGF and 10 µM Y-27632. In these conditions, the newly
698 generated NPCs can be expanded for 4-6 passages. For all the differentiation experiments we used NPCs
699 at passages 2-3.
700
701 **Assessment of long-term cell proliferation.**

702 iPSCs or NPCs were dissociated with Accutase and plated at a density of 30,000 or 50,000 cells/cm^2,
703 respectively, in the appropriate medium supplemented with 10 µM Y-27632. After 4 days, or in any case
704 at full cell confluence, cells were treated with Accutase and counted. Cells were then replated at the initial
705 density. The procedure was repeated for at least 4 passages.
706
707 **iPSC-NPCs differentiation into mixed neuronal/glial cultures**.
708 We applied a published protocol (Frati et al., 2018) with some modifications. Cells were detached using
709 Accutase and plated on Matrigel-coated dishes (20,000 cells/cm^2) in N2 medium with 20 ng/ml bFGF, 20
710 ng/ml EGF and 10 µM Y-27632 (d0). Two days after plating and for the subsequent 4 days we gradually
711 replaced N2 medium with increasing amount of Glial Differentiation Medium (GDM) containing 10 ng/ml
712 PDGF-AA, 10 ng/ml NT3, 10 ng/ml IGF-1, 5 ng/ml HGF, and 60 ng/ml T3. From d4 to the end of the
713 differentiation protocol (d24) medium was changed every other day. From d14 to day 24 cells were kept
714 in Glial Maturation Medium (GMM) in absence of growth factors and supplemented with 20 µg/ml of
715 ascorbic acid (Sigma-Aldrich).
716
717 **Lentiviral vector-mediated *hGALC* gene transfer in iPSCs.**
718 We used a previously described (Meneghini et al., 2016) third-generation lentiviral vector (LV) encoding
719 the human (h)GALC cDNA tagged with the myc peptide, under control of the human phosphoglycerate
720 kinase (PGK) promoter. The titer of the LV batch was 1.6x10^9 TU/ml. For cell transduction, iPSC colonies
721 were dissociated at single cells using Accutase and plated on Matrigel-coated 6 multi-well plates (10,000
722 cells/cm^2) in StemMACS™ iPS-Brew XF medium supplemented with 10 µM Y-27632. After 6 hours, cells
723 were incubated with LV.hGALC vector at different MOI (0-100) in StemMACS™ iPS-Brew XF medium
724 additioned with 10 µM Y-27632 and 8 µg/ml Polybrene. After an obvernight incubation, we added fresh
725 culture medium. Cells were passaged as they reached confluency, as described. Transduced cells were
726 used for the experiments after 3-4 subculturing passages, in order to dilute the non-integrated LV genome.
727
728 **Quantification of Psychosine**.
729 Psychosine quantification was performed on frozen cell pellets by TSQ Quantum AM mass spectrometer
730 (Thermo Fisher Scientific, Waltham, USA) as previously described (Lattanzi et al., 2014).
731
732 **GALC activity assay**

733 Specific beta-galactocerebrosidase activity was measured by hydrolysis of artificial fluorogenic substrate
734 4-methylumbelliferone-beta-galactopyranoside in presence of the competitive inhibitor of beta-
735 galactosidase $AgNO_3$, as previously described (Martino et al., 2009).
736
737 **PLA2 activity assay**
738 Quantification of Phospholipase A2 (PLA2) activity was performed using the EnzChek Phospholipase A2
739 Assay Kit (Thermo Fisher). 50 µl of cell lysate/well, corresponding to 20 µg total proteins, was mixed with
740 50 µl of substrate cocktail to initiate the catalytic reaction. After 10 minutes, fluorescence was measured
741 using a Victor3 Multilabel Counter (Perkin Elmer, Waltham, USA) at 360 nm (excitation) and 460 nm
742 (emission). The specific enzymatic activity was calculated for each sample and normalised for protein
743 content. Values are expressed as relative fluorescent units (RFU)/µg of protein/min.
744
745 **SA-β-Galactosidase assay (X-gal staining).**
746 Induction of senescence during NPCs differentiation was assessed with a senescence β-galactosidase (SA-
747 β-Gal) Staining Kit (Cell Signalling Technology, Danvers, USA) according to manufacturer's instructions. In
748 detail, NPCs were plated on coverslips and fixed at day 0, day 7 and day 14 days of differentiation with4%
749 PFA for 10 minutes at RT and then incubated for 24 hours with the SA-β-gal staining solution (pH=6.0) to
750 reveal SA-β-gal activity. Nuclei were then stained with Hoechst. Images were acquired using a Nikon
751 Eclipse Ni microscope, visualized and analysed using the ImageJ software. Cells displaying blue signal in
752 the cytosol were counted as positive. At least 850 nuclei/coverslip/timepoint were used for quantification.
753
754 **Proliferation analysis (EdU staining)**
755 EdU (5-ethynyl-2'-deoxyuridine), supplied with Click-iT EdU Alexa Fluor 647 Imaging Kit (Thermo-Fisher
756 Scientific), was diluted in DMSO to a final concentration of 10 mM and kept at −20°C. Cells were incubated
757 with 2µM EdU overnight in culture. $2x10^5$ cells per sample were transferred to cytometry tubes and then
758 washed with PBS 1% BSA and fixed with 100 µL of Click-iT fixative for 15 minutes. Cells were washed again
759 with PBS 1% BSA and permeabilized with 100 µL of 1X Click-iT saponin-based solution for 15 minutes.
760 Detection of EdU-DNA was performed by incubating cells with 500 µL of Click-iT Plus reaction cocktail for
761 30 minutes at RT protected from light. Cells were subsequently washed with PBS 1% BSA and fluorescence
762 was measured by flow cytometry.
763
764 **High Throughput live cell Microscopy**

765 Determination of lysosomal area was performed using a high content imaging platform in the Advanced
766 Light and Electron Microscopy Bio-Imaging Centre of San Raffaele Scientific Institute (ALEMBIC) using the
767 ArrayScan XTI HCA Reader from Thermo Fisher Scientific. Cells were plated on matrigel-coated 96 Greiner
768 Sensoplate glass bottom multiwell plates (Sigma Aldrich) (30,000 cells/well). The day after plating, cells
769 are incubated with 50 nM LysoTracker Red DND-99 (Thermo Fisher) diluted in culture medium, for 30
770 minutes at 37°C. Nuclear staining, necessary for the instrument acquisition and analysis, was performed
771 using Hoechst (5 min at room temperature, 10 µg/ml final concentration). Cells are then washed with
772 Krebs-Ringer-Hepes-bicarbonate buffer (KRH) and maintained in the same buffer for the entire duration
773 of the instrument acquisition. Thirty fields were acquired for each well; images were analysed with the
774 Thermo Scientific HCS Studio Cell Analysis Software
775
776 **Immunofluorescence.**
777 Cells are seeded in 48-multiwell plates on Matrigel-coated 10 mm round sterile glass coverslips, fixed in
778 4% PFA, rinsed with PBS, incubated with blocking solution containing 10% normal goat serum (NGS) + 0.1%
779 Triton X-100 in PBS for 45 minutes and incubated overnight at 4°C with primary antibodies diluted in
780 blocking solution. After 3 washes (10 minutes each), cells are incubated with species-specific fluorophore-
781 conjugated secondary antibodies diluted in 1% NGS in PBS for 1 hour at room temperature. Cell nuclei are
782 counterstained with Hoechst (10µg/ml, diluted in PBS). Finally, coverslips are mounted on glass slides using
783 Fluorsave mounting medium (Merck Millipore). A secondary-only control was included in every
784 experiment to confirm signal specificity. Images were obtained with a Nikon Eclipse Ni microscope,
785 visualized and analysed using the ImageJ software.
786 To evaluate DDR activation during NPCs differentiation, cells were fixed with 4% PFA for 20 min at RT and
787 then permeabilized with 0.3% Triton-X100 in PBS for 10 min. After washing, coverslips were blocked in
788 PBG (0.2% cold water fish gelatine, 0.5% BSA in PBS) for 30 min. Cells were then stained with primary
789 antibodies 1 hour at RT followed by secondary antibodies. After DAPI staining (Sigma-Aldrich), slides were
790 mounted with Aqua-Poly/mount (Polysciences Inc, Warrington, USA). Images were obtained with Leica
791 TCS SP5 confocal laser microscope and visualized with Leica Application Suite (LAS) software (Leica
792 Microsystems, Wetzlar, Germany). Quantification of DDR activation in immunofluorescence images was
793 conducted by counting colocalizing foci for 53BP1 and γH2A.X.
794 Primary and secondary antibodies used:
795
796

Primary antibodies		
Antigen	**Host species (company, catalog number)**	**Dilution**
53BP1	Rabbit polyclonal (Bethyl, A300-272A-5)	1: 600
α-fetoprotein	Mouse monoclonal (Abcam, AB3980)	1: 200
α-Smooth Muscle Actin	Mouse monoclonal (Sigma-Aldrich, C6198)	1: 400
APC	Mouse monoclonal (Calbiochem, OP80)	1: 300
β-III tubulin (TUJ1)	Mouse monoclonal (Biolegend, 801202)	1: 1,000
γH2A.X	Mouse monoclonal (Biolegend, 613402)	1: 200
Cleaved Caspase 3	Rabbit polyclonal (Cell Signaling, 9961)	1: 200
FOXG1	Rabbit polyclonal (Abcam, AB 18259)	1: 300
GALC	Mouse monoclonal, kindly provided by Dr. J.E. Deane (Univ. of Cambridge, Cambridge, UK)	1: 20
GalCer	Mouse monoclonal (Millipore MAB342)	1: 300
GFAP	Rabbit polyclonal (DAKO, ZO334)	1: 1,000
Ki67	Rabbit polyclonal (Novocastra, NCL-Ki67-p)	1: 200
NANOG	Rabbit polyclonal (Abcam, AB21624)	1: 200
Nestin	Mouse monoclonal (Millipore, MAB353)	1: 500
OCT4	Rabbit monoclonal (Abcam, AB136253)	1: 300
Olig2	Rabbit monoclonal (Abcam, AB136253)	1: 300
PAX6	Rabbit polyclonal (Covance, PRB-278P)	1: 300
TRA 1-60	Mouse monoclonal (Millipore, MAB4360	1: 100
Secondary antibodies		
Conjugate	**Host species (company, catalog number)**	**Dilution**
Alexa 488	Goat anti-mouse and Goat anti-rabbit IgG (Mol.Probes, A11001 and A11008)	1: 1,000
Alexa 546	Goat anti-mouse and Goat anti-rabbit IgG (Mol.Probes, A11003 and A11010)	1: 2,000
Alexa 568	Goat anti-rabbit IgG (Mol.Probes, A11031)	1: 2,000

Western blot analysis.

Cell pellets were lysed using RIPA buffer (50 mM Tris–HCl pH 7,4, 150 mM NaCl, 0,5% sodium deoxycholate, 0,1% SDS, 2 mM EDTA) containing protease and phosphatase inhibitors (Roche, Basel, Switzerland). Protein content was measured using the Bradford reagent (Bio-Rad, Hercules, USA) with bovine serum albumin (BSA) as the reference standard. SDS-PAGE of protein extracts was performed using Novex NuPAGE SDS-PAGE system (Thermo Fisher Scientific) according to manufacturer instructions. Proteins were transferred on PVDF membranes (Millipore, Burlington USA) for 1 hour at 400mA.

Primary and secondary antibodies used:

806

Primary antibodies		
Antigen	**Host species (company, catalog number)**	**Dilution**
α-tubulin	Mouse monoclonal (Sigma-Aldrich, T6074)	1: 5,000
Acetylated α-tubulin	Mouse monoclonal (Sigma-Aldrich, T7451)	1: 20,000
β-Actin	Rabbit polyclonal (Santa Cruz, sc-1616r)	1: 10,000
β-Actin	Mouse monoclonal (Sigma-Aldrich, A2228)	1: 10,000
β-III tubulin (TUJ1)	Mouse monoclonal (Biolegend,801202)	1: 6,000
Calnexin	Rabbit polyclonal (Sigma-Aldrich, c4731)	1: 10,000
GALC	Rabbit polyclonal (Abcam, AB137750)	1:3,000
GFAP	Mouse monoclonal (Millipore, MAB3402)	1: 100,000
LAMP1	Rabbit polyclonal (Abcam, AB24170)	1: 6,000
MYC	Rabbit polyclonal (Abcam, AB9106)	1: 15,000
Neurofilament-M (RMO 14.9)	Mouse monoclonal (Cell Signaling, 2838)	1: 1,000
OLIG1	Rabbit polyclonal (Millipore, AB5591)	1: 800
p21	Rabbit monoclonal (Cell Signaling, 2947)	1: 1,000
Polyglutamylation Modification	Mouse monoclonal (Adipogen, AG-20B-0020)	1: 5,000
SMI 311	Mouse monoclonal (Sternberg, SMI-311)	1:1000
SMI 312	Mouse monoclonal (Covance, SMI312R)	1:1000
Secondary antibodies		
Conjugate	**Host species (company, catalog number)**	**Dilution**
HRP	Goat anti-mouse IgG (Chemicon, AP124P)	1: 5,000
HRP	Goat anti-rabbit IgG (Millipore, 12-348)	1: 10,000

807

808 **Molecular analysis**

809 ***Sequencing of patient's mutations.*** Genomic DNA was extracted from iPSCs pellets using Maxwell cell
810 DNA purification Kit (Promega), following the manufacturers' instructions. DNA concentration was
811 determined by 260/280nm optical density (OD) reading on a NanoDrop ND-1000 Spectrophotometer
812 (NanoDrop, Pero, Italy). To confirm the presence of the expected mutations in the *GALC* gene of GLD
813 patients-derived cells, the regions of interests were amplified by PCR, purified from agarose gels using the
814 Wizard SV Gel and PCR Clean-Up System (Promega, Madison, USA) and sent for sequencing (to GATC
815 Services-Eurofin Genomics, Ebersberg, Germany). Sequences were checked using the Snapgene software.
816 Three primer PCR to confirm 30kb deletion in GLD1 and GLD3 cells was performed as described by (Liu et
817 al., 2011). Primers used for PCR amplification and sequencing are the following:

818

Primers for gDNA sequencing	
GALC region	**Sequence**
INTRON 11	Fw 5' - CCTATATGGAAAACAATGTGG - 3',
	Rev 5' - AAGGAGCAACATTTCAGGC - 3' (WT allele)
	Rev 5' - TCAAGTCCTTGATGATCACC - 3' (deleted allele)
EXON 4	Fw 5'- GGTGGGGAGTGAGATGGTC - 3',
	Rev 5' - CAAGGGCAAAGAAAGGATCA - 3'
EXON 8	Fw 5' - TGCTGAGACAAAAGGGCATA - 3',
	Rev 5' - GATGACGCTAACAAGGCAAA - 3'
EXON 9	Fw 5' - TTGGGTGATCCTTTTATTGTCA -3',
	Rev 5' - CACTGGCAAATCTTGCTTAAAA - 3'
EXON 14	Fw 5' - AGCAAGGAGAGCTTCTGAAGGA - 3',
	Rev 5' - AGGTTCTTGAAATAGGAGGACCA - 3'

Gene expression analysis: RT-PCR; SYBR green and TaqMan RT-PCR. Total RNA was extracted using the RNeasy Mini Kit (Qiagen). RNA was quantified by 260/280nm optical density (OD) reading on a NanoDrop ND-1000 Spectrophotometer (NanoDrop, Pero, Italy). mRNA reverse transcription (RT) is performed with QuantiTect reverse transcription kit (Qiagen, Hilden, Germany).

RT-PCR analyses were performed by using FastStart Taq DNA Polymerase, PCR KIT (Roche). For each reaction, 100 ng of template cDNA and 1 mM of primers were used. PCR products were resolved by electrophoresis in a 1,5% agarose gel.

Quantitative real time PCR reactions were performed in Optical 96-well Fast Thermal Cycling Plates (Primo 96-well plates, Euro Clone, Pero, Italy) on Viia7 quantitative real time PCR system (Applied Biosystem, Foster City, USA), using the following thermal cycling conditions:

- SYBR green qPCR: one cycle at 95°C for 2 minutes, 40 cycles at 95°C for 10 seconds and 60°C for 30 seconds; each sample is run in duplicate in a total volume of 12.5 µl/reaction, containing 6.25 µl 2X Fast SYBR Green Master Mix (Qiagen), 10 ng of template cDNA, and10µM of custom primers were used. As internal reference for normalization GAPDH was used
- TaqMan qPCR: one cycle at 95°C for 5 minutes, 40 cycles at 95°C for 50 seconds and 60°C for 1 minute. Each sample is run in duplicate in a total volume of 12.5 µl/reaction, containing 6.25 µl 2X EagleTaq Universal Master Mix (Roche), 1µl of sample cDNA and 0.63µl of Probe+Primers mix (TaqMan Gene Expression Assays, Thermo Fisher). The Viia7 software was used to extract raw data. Relative expression of mRNA for the target genes was calculated using the comparative Ct (ΔΔCt) method, with a housekeeping gene as control. Raw data (Ct values) were analyzed according to the comparative Ct method. For gene

840 expression data, analyses were performed on $2(-^{\Delta Ct})$ values relative to housekeeping gene or plotted as
841 $2^{-\Delta\Delta Ct}$ (fold change), as specified in figure legends. Primers and probes used for gene expression analyses
842 are the following:

Primers for RT-PCR	
Gene	**Sequence**
KLF4	Fw 5 ’ -ACCCACACAGGTGAGAAACCTT - 3’
	Rev 5’ - GTTGGGAACTTGACCATGATTG - 3’
SOX2	Fw 5’ - TTACCTCTTCCTCCCACTCCAG - 3’
	Rev 5’ - GGGTTTTCTCCATGCTGTTTCT - 3’
NANOG	Fw 5’- GAT CGG GCC CGC CAC CAT GAG TGT GGA TCC AGC TTG-3’
	Rev 5’- GAT CGA GCT CCA TCT TCA CAC GTC TTC AGG TTG - 3’
CD146	Fw 5’- AAG GCA ACC TCA GCC ATG TC - 3’
	Rev 5’- AGA AGA TGC GCT CGT CTT GG - 3’
CXCR4	Fw 5' - CAG CAG GTA GCA AAG TGA CG - 3'
	Rev 5' - TTG TCC GTC ATG CTT CTC AG - 3'
MAP2	Fw 5' - AAG AAG GTC GCC ATC ATA CG - 3'
	Rev 5' - GGG CTT TAG CAT GCT CTC TG - 3
PAX6	Fw 5’ - AAC AGA CAC AGC CTT CAC AAA CA - 3’
	Rev 5’ - CGG GAA CTT GAA CTG GAA CTG AC - 3’
SOX17	Fw 5’ - TTC ATG GTG TGG GCT AAG GAC - 3’
	Rev 5’ - AGT TGG GGT GGT CCT GCA TG - 3’
α-SMA	Fw 5’ - GTG TTG CCC CTG AAG AGC AT - 3’
	Rev 5’ - GCT GGG ACA TTG AAA GTC TCA - 3’
GAPDH	Fw 5' - CAG CCT CAA GAT CAT CAG CA - 3'
	Rev 5' - TGC TGT AGC CAA ATT CGT TG - 3'
Primers for SYBR-green RT-PCR	
Gene	**Sequence**
ASCL1	Fw 5' - TCCCCCAACTACTCCAACGA - 3'
	Rev 5' - GCGATCACCCTGCTTCCAAA - 3'
DCX	Fw 5' - TGGATGAAAATGAATGCCGAGT - 3'
	Rev 5' - AGCTGGAGACTTGCTTCGG - 3'
GAPDH	Fw 5' - TCAAGAAGGTGGTGAAGCAGG - 3'
	Rev 5' - ACCAGGAAATGAGCTTGACAAA - 3'
GUSB	Fw 5' - CTGACACCTCCAAGTATCCCAAG - 3'
	Rev 5' - GTCGTGTACAGAAGTACAGACCGC - 3'
IL1β	Fw 5' - GCTCAAGTGTCTGAAGCAGCC - 3'
	Rev 5' - CAGCTTCAAAGAACAAGTCATCCT - 3'

NANOG	Fw 5' - ATGCCTCACACGGAGACTGT - 3'
	Rev 5' - AAGTGGGTTGTTTGCCTTTG - 3'
OCT4	Fw 5' - TCGAGAACCGAGTGAGAGG - 3'
	Rev 5' - GAACCACACTCGGACCACA - 3'
PAX6	Fw 5' - AGTGAATCAGCTCGGTGGTGTCTT - 3'
	Rev 5’ - TGCAGAATTCGGGAAATGTCGC - 3'
TNF-α	Fw 5' – CCAGGGACCTCTCTCTAATCAGC - 3'
	Rev 5’ – GGTTTGCTACAACATGGGCTAC - 3'
Probe+Primers for Taqman RT-PCR	
Gene	**Commercial Code**
DCX	Hs00167057_m1
GALC	Hs01012300_m1
GAPDH	Hs02758991_g1
GFAP	Hs00157674_m1
KLF4	Hs00358836_m1
NANOG	Hs02387400_g1
OLIG2	Hs00300164_s1
OCT4	Hs03005111_g1
SOX2	Hs01053049_s1

Determination of vector copy number (VCN)

Genomic DNA was extracted from cell pelletes using Maxwell cell DNA purification Kit (Promega) or QIAamp DNA Micro Kit (Quiagen), depending on the number of cells. The number of integrated vector copies/genome was quantified by TaqMan analysis, as previously described (Lattanzi et al., 2010). Briefly, quantitative PCR was performed on 50 ng of template DNA using probes and primers that anneal to the PSI (ψ) sequence of the LV backbone and to a fragment of the human telomerase gene. A standard curve was set up with gDNA extracted from a human lymphoblast cell line (CEM) carrying 1 copy of integrated LV.GFP, validated by Southern blot analysis. The standard curve, based on different dilutions of CEM gDNA (from 0,32 ng to 40 ng) was used for both LV and telomerase amplification. Reactions were carried out in a total volume of 25 µl, on Viia7 quantitative real time PCR system (Applied Biosystem). Eventually, VCN is calculated as: (ng LV/ng endogenous DNA) × (number of LV integrations in the standard curve) × cell ploidy. Primers and probes used for VCN analyses are the following:

Primers for VCN assay		
Gene	**Probe sequence**	**Primer sequence**
HIV	5’- ATCTCTCTCCTTCTAGCCTC - 3’	For 5’ – TACTGACGCTCTCGCACC - 3’
		Rev 5’ – TCTCGACGCAGGACTCG - 3’

TELO	5' -TCAGGACGTCGAGTGGACACGGTG- 3'	For 5' – GGCACACGTGGCTTTTCG - 3'
		Rev 5' – GGTGAACCTCGTAAGTTTATGCAA - 3'

Lipidomic analyses

Lipid extraction. Cell pellets were resuspended in 150 mM Ammonium bicarbonate and passed through a 26G syringe needle to prepare cell lysate. Lipids were extracted starting from an equivalent of 10 µg of proteins, using a 2 steps extraction protocol (Folch method) with methanol and chloroform in different proportions (FOLCH et al., 1957). Organic phase fractions were then dried out and resuspended in 50 µL of CH3OH for subsequent analysis. Before extraction, samples were spiked in with 16 internal standards: PC (12:0/13:0) 40 pmol, PE (12:0/13:0) 52 pmol, PG (12:0/13:0) 7.5 pmol, PS (12:0/13:0) 43 pmol, PI (12:0/13:0) 54 pmol, Cer (d18:1/25:0) 100 pmol, CE(19:0) 100 pmol, GlcCer (d18:1/12:0) 50 pmol, LacCer (d18:1/12:0) 50 pmol, Sphinganine (d17:0) 50 pmol, Sphingosine-1-P (d17:1) 100 pmol, Sphingosine (d17:1) 50 pmol, Galactosyl(ß) Sphingosine-d5 20 pmol, d5-TG ISTD Mix I 20 pmol, d5-DG ISTD Mix I 20 pmol, cholesterol (d7) 800 pmol.

Protein quantification. Proteins were extracted form 20 µL of ammonium bicarbonate resuspended fractions by adding 5 µL of lysis buffer (10% NP40, 2%SDS in PBS) and quantified by BCA protein assay kit (ThermoFisher Scientific, 23225).

Lipid profiling data acquisition. Lipids extracts were diluted 1:5 with 95% mobile phase A (CH3CN:H2O 40:60; 5mM NH4COOCH3; 0.1% FA) plus 5% mobile phase B (IPA:H2O 90:10; 5mM NH4COOCH3; 0.1% FA) and 1 µL injected on a liquid chromatography system nLC Ekspert nanoLC400 (Eksigent, 5033460C; Singapore) coupled with a Triple TOF 6600 (AB Sciex; Singapore). Chromatography was performed using an in house packed nanocolumn Kinetex EVO C18, 1.7 µm, 100 A, 0.75 x 100 mm. The gradient elution at flow rate of 150 nL/min was initially started from 5 % of mobile phase B, linearly increased to 100 % B in 5 min, maintained for 45 min, then returned to the initial ratio in 2 min and maintained for 8 min. Positive mode acquisition in MS was performed with the following parameters: mass over charge (m/z) range 100–1700, T source 80C, Ion Spray Voltage 2000, Declustering Potential (DP) 80, fixed collision energy 40 V (+). For IDA analysis (Top 8), range of m/z was set as 200–1800 in positive ion mode, target ions were excluded for 20 sec after 2 occurrences (Analyst TF 1.7.1).

Data processing and analysis. Lipidview workstation (version 1.3 beta, AB SCIEX, USA) was used for lipids identification and quantitation. Lipid identification was based on exact mass, retention time, and MS/MS pattern. Lipid species based on precursor fragment ion pairs were determined using a comprehensive target list in LipidView (Sciex). Lipid species identification was performed using; the mass tolerance of 0.05 in MS and 0.02 in MS/MS, s/n of 3 and % peak intensity > 0 for positive ion mode.

Lipid classes included for statistics and downstream analysis were: cholesterol ester (CE), sphingomyelin (SM), diacylglycerol (DAG), triacylglycerol (TAG), ceramide (Cer) phosphatidylcholine (PC), phosphatidylethanolamine (PE), phosphatidylglycerol (PG), phosphatidylinositol (PI), phosphatidylserine (PS) and lysophosphatidylcholine (LPC), lysophosphatidylethanolamine (LPE), lysophosphatidylglycerol (LPG), lysophosphatidylinositol (LPI), lysophosphatidylserine (LPS), hexosylceramide (HexCer), dihexosylceramide (Hex2Cer), trihexosylceramide (Hex3Cer), sulphatides (SGalCer), ceramide-phosphate (CerP), in positive mode.

Statistics

Data were analysed with Graph Pad Prism version 8 for Macintosh and expressed as the mean ± standard error of the mean (SEM). The number of samples and the statistical tests and post-tests used are specified in the legends to each figure. $p<0.05$ was considered statistically significant.

For lipid analyses, statistical analysis was performed using Metaboanalyst 4.0 web tool https://www.metaboanalyst.ca/MetaboAnalyst/faces/home.xhtml (Chong et al., 2018).

902 **References**

903 Allende, M.L., Cook, E.K., Larman, B.C., Nugent, A., Brady, J.M., Golebiowski, D., Sena-Esteves, M., Tifft,
904 C.J., and Proia, R.L. (2018). Cerebral organoids derived from Sandhoff disease-induced pluripotent stem
905 cells exhibit impaired neurodifferentiation. J. Lipid Res. *59*, 550-563.
906 Allewelt, H.B., Page, K., Taskindoust, M., Troy, J.D., Wood, S., Parikh, S., Prasad, V.K., and Kurtzberg, J.
907 (2016). Long-term functional outcomes following hematopoietic stem cell transplantation for krabbe
908 disease. Biol. Blood Marrow Transplant. *22*, S102–S103.
909 Ballabio, A., and Gieselmann, V. (2009). Lysosomal disorders: from storage to cellular damage. Biochim
910 Biophys Acta *1793*, 684–696.
911 Bayó-Puxan, N., Terrasso, A.P., Creyssels, S., Simão, D., Begon-Pescia, C., Lavigne, M., Salinas, S., Bernex,
912 F., Bosch, A., Kalatzis, V., et al. (2018). Lysosomal and network alterations in human
913 mucopolysaccharidosis type VII iPSC-derived neurons. Sci. Rep. *8*, 16644.
914 Berardi, A.S., Pannuzzo, G., Graziano, A., Costantino-Ceccarini, E., Piomboni, P., and Luddi, A. (2014).
915 Pharmacological chaperones increase residual beta-galactocerebrosidase activity in fibroblasts from
916 krabbe patients. Mol. Genet. Metab. *112*, 294–301.
917 Bieberich, E. (2012). It's a lipid's world: Bioactive lipid metabolism and signaling in neural stem cell
918 differentiation. Neurochem. Res. *37*,1208-1229.
919 Biffi, A., Montini, E., Lorioli, L., Cesani, M., Fumagalli, F., Plati, T., Baldoli, C., Martino, S., Calabria, A., Canale,
920 S., et al. (2013). Lentiviral hematopoietic stem cell gene therapy benefits metachromatic
921 leukodystrophy. Science (80-.). *341*, 1233158.
922 Bongarzone, E.R. oque, Escolar, M.L. uisa, Gray, S.J. ames, Kafri, T., Vite, C.H. erman, and Sands, M.S. teven
923 (2016). Insights into the Pathogenesis and Treatment of Krabbe Disease. Pediatr. Endocrinol. Rev. *13*,
924 689–696.
925 Borda, J.T., Alvarez, X., Mohan, M., Ratterree, M.S., Phillippi-Falkenstein, K., Lackner, A. a, and Bunnell, B.
926 a (2008). Clinical and immunopathologic alterations in rhesus macaques affected with globoid cell
927 leukodystrophy. Am J Pathol *172*, 98–111.
928 Bradbury, A.M., Rafi, M.A., Bagel, J.H., Brisson, B.K., Marshall, M.S., Pesayco Salvador, J., Jiang, X., Swain,
929 G.P., Prociuk, M.L., Odonnell, P.A., et al. (2018). AAVrh10 Gene Therapy Ameliorates Central and
930 Peripheral Nervous System Disease in Canine Globoid Cell Leukodystrophy (Krabbe Disease). Hum.
931 Gene Ther. *29,* 785-801.
932 Buratta, S., Urbanelli, L., Sagini, K., Giovagnoli, S., Caponi, S., Fioretto, D., Mitro, N., Caruso, D., and Emiliani,
933 C. (2017). Extracellular vesicles released by fibroblasts undergoing H-Ras induced senescence show

934 changes in lipid profile. PLoS One *12*, e0188840.
935 Canals, I., Soriano, J., Orlandi, J.G., Torrent, R., Richaud-Patin, Y., Jim??nez-Delgado, S., Merlin, S., Follenzi,
936 A., Consiglio, A., Vilageliu, L., et al. (2015). Activity and high-order effective connectivity alterations in
937 sanfilippo C patient-specific neuronal networks. Stem Cell Reports *5*, 546–557.
938 Castelvetri, L.C., Givogri, M.I., Zhu, H., Smith, B., Lopez-Rosas, A., Qiu, X., van Breemen, R., and Bongarzone,
939 E.R. (2011). Axonopathy is a compounding factor in the pathogenesis of Krabbe disease. Acta
940 Neuropathol *122*, 35-48.
941 Chambers, S.M., Fasano, C.A., Papapetrou, E.P., Tomishima, M., Sadelain, M., and Studer, L. (2009). Highly
942 efficient neural conversion of human ES and iPS cells by dual inhibition of SMAD signaling. Nat.
943 Biotechnol. *27*, 275–280.
944 Chambers, S.M., Mica, Y., Studer, L., and Tomishima, M.J. (2011). Converting human pluripotent stem cells
945 to neural tissue and neurons to model neurodegeneration. Methods Mol. Biol. *793*, 87–97.
946 Chong, J., Soufan, O., Li, C., Caraus, I., Li, S., Bourque, G., Wishart, D.S., and Xia, J. (2018). MetaboAnalyst
947 4.0: Towards more transparent and integrative metabolomics analysis. Nucleic Acids Res. *46*, W486-
948 W494.
949 Claus, R., Dorer, M., Bunck, A., and Deigner, H. (2009). Inhibition of Sphingomyelin Hydrolysis: Targeting
950 the Lipid Mediator Ceramide as a Key Regulator of Cellular Fate. Curr. Med. Chem. *16*, 1978-2000.
951 Duffner, P.K., Barczykowski, A., Jalal, K., Yan, L., Kay, D.M., and Carter, R.L. (2011). Early infantile Krabbe
952 disease: Results of the world-wide Krabbe registry. Pediatr. Neurol. *45*, 141–148.
953 Duffner, P.K., Barczykowski, A., Kay, D.M., Jalal, K., Yan, L., Abdelhalim, A., Gill, S., Gill, A.L., and Carter, R.
954 (2012). Later onset phenotypes of Krabbe disease: Results of the world-wide registry. Pediatr. Neurol.
955 *46*, 298–306.
956 Escolar, M.L., Kiely, B.T., Shawgo, E., Hong, X., Gelb, M.H., Orsini, J.J., Matern, D., and Poe, M.D. (2017).
957 Psychosine, a marker of Krabbe phenotype and treatment effect. Mol. Genet. Metab. *121*, 271-278.
958 Folch, J., Lees, M., and Sloane Stanley, G.H. (1957). A simple method for the isolation and purification of
959 total lipides from animal tissues. J. Biol. Chem. *226*, 497-509.
960 Folts, C.J., Scott-Hewitt, N., Pröschel, C., Mayer-Pröschel, M., and Noble, M. (2016). Lysosomal Re-
961 acidification Prevents Lysosphingolipid-Induced Lysosomal Impairment and Cellular Toxicity. PLoS Biol.
962 *14*.
963 Frati, G., Luciani, M., Meneghini, V., De Cicco, S., Ståhlman, M., Blomqvist, M., Grossi, S., Filocamo, M.,
964 Morena, F., Menegon, A., et al. (2018). Human iPSC-based models highlight defective glial and neuronal
965 differentiation from neural progenitor cells in metachromatic leukodystrophy. Cell Death Dis. *9*, 698.

Gama Sosa, M.A., de Gasperi, R., Undevia, S., Yeretsian, J., Rouse 2nd, S.C., Lyerla, T.A., and Kolodny, E.H. (1996). Correction of the galactocerebrosidase deficiency in globoid cell leukodystrophy-cultured cells by SL3-3 retroviral-mediated gene transfer. Biochem Biophys Res Commun *218*, 766–771.

De Gasperi, R., Gama Sosa, M.A., Sartorato, E.L., Battistini, S., MacFarlane, H., Gusella, J.F., Krivit, W., and Kolodny, E.H. (1996). Molecular heterogeneity of late-onset forms of globoid-cell leukodystrophy. Am. J. Hum. Genet. *59*, 1233–1242.

De Gasperi, R., Gama Sosa, M.A., Sartorato, E., Battistini, S., Raghavan, S., and Kolodny, E.H. (1999). Molecular basis of late-life globoid cell leukodystrophy. Hum Mutat *14*, 256–262.

Gentner, B., Visigalli, I., Hiramatsu, H., Lechman, E., Ungari, S., Giustacchini, A., Schira, G., Amendola, M., Quattrini, A., Martino, S., et al. (2010). Identification of hematopoietic stem cell-specific miRNAs enables gene therapy of globoid cell leukodystrophy. Sci. Transl. Med. *2*, 58ra84.

Giri, S., Khan, M., Rattan, R., Singh, I., and Singh, A.K. (2006). Krabbe disease: psychosine-mediated activation of phospholipase A2 in oligodendrocyte cell death. J Lipid Res *47*, 1478–1492.

Graziano, A.C.E., and Cardile, V. (2015). History, genetic, and recent advances on Krabbe disease. Gene. *555(1),* 2-13

Del Grosso, A., Angella, L., Tonazzini, I., Moscardini, A., Giordano, N., Caleo, M., Rocchiccioli, S., and Cecchini, M. (2019). Dysregulated autophagy as a new aspect of the molecular pathogenesis of Krabbe disease. Neurobiol. Dis. *129*, 195-207.

Gupta, A., Poe, M.D., Styner, M.A., Panigrahy, A., and Escolar, M.L. (2015). Regional differences in fiber tractography predict neurodevelopmental outcomes in neonates with infantile Krabbe disease. NeuroImage Clin. *7*, 792–798.

Hannun, Y.A., and Obeid, L.M. (2002). The ceramide-centric universe of lipid-mediated cell regulation: Stress encounters of the lipid kind. J. Biol. Chem. *277*, 25847-25850.

Hannun, Y.A., and Obeid, L.M. (2008). Principles of bioactive lipid signalling: Lessons from sphingolipids. Nat Rev Mol Cell Biol *9*, 139–150.

Hannun, Y.A., and Obeid, L.M. (2017). Sphingolipids and their metabolism in physiology and disease. Nat. Rev. Mol. Cell Biol. *19*, 175-191.

Hawkins-Salsbury, J. a, Parameswar, A.R., Jiang, X., Schlesinger, P.H., Bongarzone, E., Ory, D.S., Demchenko, A. V, and Sands, M.S. (2013). Psychosine, the cytotoxic sphingolipid that accumulates in globoid cell leukodystrophy, alters membrane architecture. J. Lipid Res. *54*, 3303–3311.

Hawkins-Salsbury, J.A., Shea, L., Jiang, X., Hunter, D.A., Guzman, A.M., Reddy, A.S., Qin, E.Y., Li, Y., Gray, S.J., Ory, D.S., et al. (2015). Mechanism-based combination treatment dramatically increases

998 therapeutic efficacy in murine globoid cell leukodystrophy. J. Neurosci. *35*, 6495–6505.
999 He, S., and Sharpless, N.E. (2017). Senescence in Health and Disease. Cell. *169*, 1000-1011.
1000 Higuchi, T., Kawagoe, S., Otsu, M., Shimada, Y., Kobayashi, H., Hirayama, R., Eto, K., Ida, H., Ohashi, T.,
1001 Nakauchi, H., et al. (2014). The generation of induced pluripotent stem cells (iPSCs) from patients with
1002 infantile and late-onset types of Pompe disease and the effects of treatment with acid-??-glucosidase
1003 in Pompe's iPSCs. Mol. Genet. Metab. *112*, 44–48.
1004 Huang, H.-P., Chuang, C.-Y., and Kuo, H.-C. (2012). Induced pluripotent stem cell technology for disease
1005 modeling and drug screening with emphasis on lysosomal storage diseases. Stem Cell Res. Ther. *3*, 34.
1006 Igisu, H., and Suzuki, K. (1984). Progressive accumulation of toxic metabolite in a genetic leukodystrophy.
1007 Science (80-.). *224*, 753–755.
1008 Irahara-Miyana, K., Otomo, T., Kondo, H., Hossain, M.A., Ozono, K., and Sakai, N. (2018). Unfolded protein
1009 response is activated in Krabbe disease in a manner dependent on the mutation type. J. Hum. Genet.
1010 *63*, 699–706.
1011 Jalal, K., Carter, R., Yan, L., Barczykowski, A., and Duffner, P.K. (2012). Does galactocerebrosidase activity
1012 predict krabbe phenotype? Pediatr. Neurol. *47*, 324–329.
1013 Jana, A., Hogan, E.L., and Pahan, K. (2009). Ceramide and neurodegeneration: Susceptibility of neurons
1014 and oligodendrocytes to cell damage and death. J. Neurol. Sci. *278*, 5-15.
1015 Jatana, M., Giri, S., and Singh, A.K. (2002). Apoptotic positive cells in Krabbe brain and induction of
1016 apoptosis in rat C6 glial cells by psychosine. Neurosci Lett *330*, 183–187.
1017 Kobolák, J., Molnár, K., Varga, E., Bock, I., Jezsó, B., Téglási, A., Zhou, S., Lo Giudice, M., Hoogeveen-
1018 Westerveld, M., Pijnappel, W.P., et al. (2019). Modelling the neuropathology of lysosomal storage
1019 disorders through disease-specific human induced pluripotent stem cells. Exp. Cell Res. *380*, 216-233.
1020 Lattanzi, A., Neri, M., Maderna, C., di Girolamo, I., Martino, S., Orlacchio, A., Amendola, M., Naldini, L., and
1021 Gritti, A. (2010). Widespread enzymatic correction of CNS tissues by a single intracerebral injection of
1022 therapeutic lentiviral vector in leukodystrophy mouse models. Hum. Mol. Genet. *19*, 2208–2227.
1023 Lattanzi, A., Salvagno, C., Maderna, C., Benedicenti, F., Morena, F., Kulik, W., Naldini, L., Montini, E.,
1024 Martino, S., and Gritti, A. (2014). Therapeutic benefit of lentiviral-mediated neonatal intracerebral gene
1025 therapy in a mouse model of globoid cell leukodystrophy. Hum. Mol. Genet. *23*, 3250–3268.
1026 Lee, S.J., Yi, T., Ahn, S.H., Lim, D.K., Hong, J.Y., Cho, Y.K., Lim, J., Song, S.U., and Kwon, S.W. (2014).
1027 Senescing human bone-marrow-derived clonal mesenchymal stem cells have altered lysophospholipid
1028 composition and functionality. J. Proteome Res. *13*, 1438-1449.
1029 Lee, W.C., Kang, D., Causevic, E., Herdt, A.R., Eckman, E.A., and Eckman, C.B. (2010). Molecular

1030 characterization of mutations that cause globoid cell leukodystrophy and pharmacological rescue using
1031 small molecule chemical chaperones. J Neurosci *30*, 5489–5497.
1032 Lemonnier, T., Blanchard, S., Toli, D., Roy, E., Bigou, S., Froissart, R., Rouvet, I., Vitry, S., Heard, J.M., and
1033 Bohl, D. (2011). Modeling neuronal defects associated with a lysosomal disorder using patient-derived
1034 induced pluripotent stem cells. Hum. Mol. Genet. *20*, 3653–3666.
1035 Lin, D., Fantz, C.R., Levy, B., Rafi, M.A., Vogler, C., Wenger, D.A., and Sands, M.S. (2005). AAV2/5 vector
1036 expressing galactocerebrosidase ameliorates CNS disease in the murine model of globoid-cell
1037 leukodystrophy more efficiently than AAV2. Mol Ther *12*, 422–430.
1038 Liu, Y., Gibson, J., Wheeler, J., Kwee, L.C., Santiago-Turla, C.M., Akafo, S.K., Lichter, P.R., Gaasterland, D.E.,
1039 Moroi, S.E., Challa, P., et al. (2011). GALC deletions increase the risk of primary Open-Angle Glaucoma:
1040 The role of mendelian variants in complex disease. PLoS One. *6*, e27134.
1041 Lizardo, D.Y., Lin, Y.L., Gokcumen, O., and Atilla-Gokcumen, G.E. (2017). Regulation of lipids is central to
1042 replicative senescence. Mol. Biosyst. *13*, 498-509.
1043 Lizardo, D.Y., Parisi, L.R., Li, N., and Atilla-Gokcumen, G.E. (2018). Noncanonical Roles of Lipids in Different
1044 Cellular Fates. Biochemistry. *57*, 22-29.
1045 Lojewski, X., Staropoli, J.F., Biswas-Legrand, S., Simas, A.M., Haliw, L., Selig, M.K., Coppel, S.H., Goss, K.A.,
1046 Petcherski, A., Chandrachud, U., et al. (2014). Human iPSC models of neuronal ceroid lipofuscinosis
1047 capture distinct effects of TPP1 and CLN3 mutations on the endocytic pathway. Hum. Mol. Genet. *23*,
1048 2005–2022.
1049 Luni, C., Gagliano, O., and Elvassore, N. (2016). Microfluidic technology enhances the potential of human
1050 pluripotent stem cells. Biochem. Biophys. Res. Commun. *473*, 10–14.
1051 Luzi, P., Rafi, M.A., and Wenger, D.A. (1995). Characterization of the large deletion in the GALC gene found
1052 in patients with Krabbe disease. Hum. Mol. Genet. *4*, 2335–2338.
1053 Luzi, P., Rafi, M.A., Victoria, T., Baskin, G.B., and Wenger, D.A. (1997). Characterization of the rhesus
1054 monkey galactocerebrosidase (GALC) cDNA and gene and identification of the mutation causing globoid
1055 cell leukodystrophy (Krabbe disease) in this primate. Genomics *42*, 319–324.
1056 Maetzel, D., Sarkar, S., Wang, H., Abi-Mosleh, L., Xu, P., Cheng, A.W., Gao, Q., Mitalipova, M., and Jaenisch,
1057 R. (2014). Genetic and chemical correction of cholesterol accumulation and impaired autophagy in
1058 hepatic and neural cells derived from niemann-pick type C patient-specific iPS cells. Stem Cell Reports
1059 *2*, 866–880.
1060 Martino, S., Tiribuzi, R., Tortori, A., Conti, D., Visigalli, I., Lattanzi, A., Biffi, A., Gritti, A., and Orlacchio, A.
1061 (2009). Specific determination of beta-galactocerebrosidase activity via competitive inhibition of beta-

galactosidase. Clin. Chem. *55*, 541–548.

Meneghini, V., Lattanzi, A., Tiradani, L., Bravo, G., Morena, F., Sanvito, F., Calabria, A., Bringas, J., Fisher-Perkins, J.M., Dufour, J.P., et al. (2016). Pervasive supply of therapeutic lysosomal enzymes in the CNS of normal and Krabbe-affected non-human primates by intracerebral lentiviral gene therapy. EMBO Mol. Med. *8*, 489–510.

Meneghini, V., Frati, G., Sala, D., De Cicco, S., Luciani, M., Cavazzin, C., Paulis, M., Mentzen, W., Morena, F., Giannelli, S., et al. (2017). Generation of Human Induced Pluripotent Stem Cell-Derived Bona Fide Neural Stem Cells for Ex Vivo Gene Therapy of Metachromatic Leukodystrophy. Stem Cells Transl. Med. *6*, 352–368.

Misslin, C., Velasco-Estevez, M., Albert, M., O'Sullivan, S.A., and Dev, K.K. (2017). Phospholipase A2 is involved in galactosylsphingosine-induced astrocyte toxicity, neuronal damage and demyelination. PLoS One. *12*, e0187217.

Mullen, T.D., Hannun, Y.A., Obeid, L.M., Hannun, Y.A., Obeid, L.M., Gatt, S., Gatt, S., Yavin, E., Gatt, S., Sribney, M., et al. (2012). Ceramide synthases at the centre of sphingolipid metabolism and biology. Biochem. J. *441*, 139–150.

Nicaise, A.M., Wagstaff, L.J., Willis, C.M., Paisie, C., Chandok, H., Robson, P., Fossati, V., Williams, A., and Crocker, S.J. (2019). Cellular senescence in progenitor cells contributes to diminished remyelination potential in progressive multiple sclerosis. Proc. Natl. Acad. Sci. U. S. A. *116*, 9030-9039.

Ordoñez, M.P., and Steele, J.W. (2016). Modeling Niemann Pick type C1 using human embryonic and induced pluripotent stem cells. Brain Res. *1656*, 63-67.

Panicker, L.M., Miller, D., Park, T.S., Patel, B., Azevedo, J.L., Awad, O., Masood, M.A., Veenstra, T.D., Goldin, E., Stubblefield, B.K., et al. (2012). Induced pluripotent stem cell model recapitulates pathologic hallmarks of Gaucher disease. Proc. Natl. Acad. Sci. U. S. A. *109*, 18054–18059.

Pellegrini, D., Del Grosso, A., Angella, L., Giordano, N., Dilillo, M., Tonazzini, I., Caleo, M., Cecchini, M., and McDonnell, L.A. (2019). Quantitative microproteomics based characterization of the central and peripheral nervous system of a mouse model of Krabbe disease. Mol. Cell. Proteomics. *8*, 1227-1241.

Potter, G.B., and Petryniak, M.A. (2016). Neuroimmune mechanisms in Krabbe's disease. J. Neurosci. Res. *94*, 1341-1348.

Potter, G.B., Santos, M., Davisson, M.T., Rowitch, D.H., Marks, D.L., Bongarzone, E.R., and Petryniak, M.A. (2013). Missense mutation in mouse GALC mimics human gene defect and offers new insights into Krabbe disease. Hum Mol Genet *22*, 3397–3414.

Rafi, M.A., Luzi, P., Chen, Y.Q., and Wenger, D.A. (1995). A large deletion together with a point mutation

in the GALC gene is a common mutant allele in patients with infantile krabbe disease. Hum. Mol. Genet. *4*, 1285–1289.

Rafi, M.A., Fugaro, J., Amini, S., Luzi, P., de Gala, G., Victoria, T., Dubell, C., Shahinfar, M., and Wenger, D.A. (1996). Retroviral vector-mediated transfer of the galactocerebrosidase (GALC) cDNA leads to overexpression and transfer of GALC activity to neighboring cells. Biochem Mol Med *58*, 142–150.

Rafi, M.A., Rao, H.Z., Luzi, P., and Wenger, D.A. (2015). Long-term Improvements in Lifespan and Pathology in CNS and PNS After BMT Plus One Intravenous Injection of AAVrh10-GALC in Twitcher Mice. Mol. Ther. *23*, 1681–1690.

Ribbens, J., Whiteley, G., Furuya, H., Southall, N., Hu, X., Marugan, J., Ferrer, M., and Maegawa, G.H.B. (2013). A high-throughput screening assay using Krabbe disease patient cells. Anal. Biochem. *434*, 15–25.

Ricca, A., and Gritti, A. (2016). Perspective on innovative therapies for globoid cell leukodystrophy. J. Neurosci. Res. *94*, 1304–1317.

Ricca, A., Rufo, N., Ungari, S., Morena, F., Martino, S., Kulik, W., Alberizzi, V., Bolino, A., Bianchi, F., Del Carro, U., et al. (2015). Combined gene/cell therapies provide long-term and pervasive rescue of multiple pathological symptoms in a murine model of globoid cell leukodystrophy. Hum. Mol. Genet. *24*, 3372–3389.

Samie, M.A., and Xu, H. (2014). Lysosomal exocytosis and lipid storage disorders. J. Lipid Res. *55*, 995–1009.

Santambrogio, S., Ricca, A., Maderna, C., Ieraci, A., Aureli, M., Sonnino, S., Kulik, W., Aimar, P., Bonfanti, L., Martino, S., et al. (2012). The galactocerebrosidase enzyme contributes to maintain a functional neurogenic niche during early post-natal CNS development. Hum. Mol. Genet. *21*, 4732–4750.

Sessa, M., Lorioli, L., Fumagalli, F., Acquati, S., Redaelli, D., Baldoli, C., Canale, S., Lopez, I.D., Morena, F., Calabria, A., et al. (2016). Lentiviral haemopoietic stem-cell gene therapy in early-onset metachromatic leukodystrophy: an ad-hoc analysis of a non-randomised, open-label, phase 1/2 trial. Lancet *388*, 476–487.

Shi, Y., Inoue, H., Wu, J.C., and Yamanaka, S. (2017). Induced pluripotent stem cell technology: a decade of progress. Nat. Rev. Drug Discov. *16*, 115–130.

Shin, D., Feltri, M.L., and Wrabetz, L. (2016). Altered Trafficking and Processing of GALC Mutants Correlates with Globoid Cell Leukodystrophy Severity. J. Neurosci. *36*, 1858–1870.

Smith, B.R., Santos, M.B., Marshall, M.S., Cantuti-Castelvetri, L., Lopez-Rosas, A., Li, G., Van Breemen, R., Claycomb, K.I., Gallea, J.I., Celej, M.S., et al. (2014). Neuronal inclusions of α-synuclein contribute to

the pathogenesis of Krabbe disease. J. Pathol. *232*, 509–521.

Son, M.-Y., Kwak, J.E., Seol, B., Lee, D.Y., Jeon, H., and Cho, Y.S. (2015). A novel human model of the neurodegenerative disease GM1 gangliosidosis using induced pluripotent stem cells demonstrates inflammasome activation. J. Pathol. *237*, 98-110.

Spratley, S.J., Hill, C.H., Viuff, A.H., Edgar, J.R., Skjødt, K., and Deane, J.E. (2016). Molecular Mechanisms of Disease Pathogenesis Differ in Krabbe Disease Variants. Traffic *17*, 908–922.

Sun, Y., Florer, J., Mayhew, C.N., Jia, Z., Zhao, Z., Xu, K., Ran, H., Liou, B., Zhang, W., Setchell, K.D.R., et al. (2015). Properties of neurons derived from induced pluripotent stem cells of Gaucher disease type 2 patient fibroblasts: Potential role in neuropathology. PLoS One *10*.

Suzuki, K. (1983). The twitcher mouse. A model of human globoid cell leukodystrophy (krabbe's disease). Am J Pathol *111*, 394–397.

Suzuki, K., and Suzuki, Y. (1970). Globoid cell leucodystrophy (Krabbe's disease): deficiency of galactocerebroside beta-galactosidase. Proc Natl Acad Sci U S A *66*, 302–309.

Tappino, B., Biancheri, R., Mort, M., Regis, S., Corsolini, F., Rossi, A., Stroppiano, M., Lualdi, S., Fiumara, A., Bembi, B., et al. (2010). Identification and characterization of 15 novel GALC gene mutations causing Krabbe disease. Hum. Mutat. *31*, E1894-1914.

Teixeira, C.A., Miranda, C.O., Sousa, V.F., Santos, T.E., Malheiro, A.R., Solomon, M., Maegawa, G.H., Brites, P., and Sousa, M.M. (2014). Early axonal loss accompanied by impaired endocytosis, abnormal axonal transport, and decreased microtubule stability occur in the model of Krabbe's disease. Neurobiol. Dis. *66*, 92–103.

Tiscornia, G., Lorenzo Vivas, E., Matalonga, L., Berniakovich, I., Barragán Monasterio, M., Eguizábal, C., Gort, L., González, F., Ortiz mellet, C., García Fernández, J.M., et al. (2013). Neuronopathic Gaucher's disease: Induced pluripotent stem cells for disease modelling and testing chaperone activity of small compounds. Hum. Mol. Genet. *22*, 633–645.

Trayssac, M., Hannun, Y.A., and Obeid, L.M. (2018). Role of sphingolipids in senescence: Implication in aging and age-related diseases. J. Clin. Invest. *128*, 2702-2712.

Trilck, M., Hübner, R., Seibler, P., Klein, C., Rolfs, A., and Frech, M.J. (2013). Niemann-Pick type C1 patient-specific induced pluripotent stem cells display disease specific hallmarks. Orphanet J. Rare Dis. *8*, 144.

Ungari, S., Montepeloso, A., Morena, F., Cocchiarella, F., Recchia, A., Martino, S., Gentner, B., Naldini, L., and Biffi, A. (2015). Design of a regulated lentiviral vector for hematopoietic stem cell gene therapy of globoid cell leukodystrophy. Mol. Ther. Methods Clin. Dev. *2*, 15038.

Vallejo-Diez, S., Fleischer, A., Martín-Fernández, J.M., Sánchez-Gilabert, A., and Bachiller, D. (2018).

1158 Generation of two induced pluripotent stem cells lines from a Mucopolysaccharydosis IIIB (MPSIIIB)
1159 patient. Stem Cell Res. *33*, 180-184.
1160 Venable, M.E., Lee, J.Y., Smyth, M.J., Bielawska, A., and Obeid, L.M. (1995). Role of ceramide in cellular
1161 senescence. J. Biol. Chem. *270*, 30701-30708.
1162 Wenger, D.A. (2000). Murine, canine and non-human primate models of Krabbe disease. Mol. Med. Today
1163 *6*, 449–451.
1164 Wenger, D.A., and Luzi, P. (2014). Krabbe Disease: Globoid Cell Leukodystrophy. In Rosenberg's Molecular
1165 and Genetic Basis of Neurological and Psychiatric Disease: Fifth Edition, pp. 337–346.
1166 White, A.B., Givogri, M.I., Lopez-Rosas, A., Cao, H., van Breemen, R., Thinakaran, G., and Bongarzone, E.R.
1167 (2009). Psychosine accumulates in membrane microdomains in the brain of krabbe patients, disrupting
1168 the raft architecture. J Neurosci *29*, 6068–6077.
1169 White, A.B., Galbiati, F., Givogri, M.I., Lopez Rosas, A., Qiu, X., Van Breemen, R., and Bongarzone, E.R.
1170 (2011). Persistence of psychosine in brain lipid rafts is a limiting factor in the therapeutic recovery of a
1171 mouse model for Krabbe disease. J. Neurosci. Res. *89*, 352–364.
1172 Yamanaka, S. (2007). Strategies and new developments in the generation of patient-specific pluripotent
1173 stem cells. Cell Stem Cell *1*, 39–49.
1174 Young, M.M., and Wang, H.G. (2018). Sphingolipids as Regulators of Autophagy and Endocytic Trafficking.
1175 Adv. Cancer Res. *140*, 27-60.
1176 Young, S.A., Mina, J.G., Denny, P.W., and Smith, T.K. (2012). Sphingolipid and ceramide homeostasis:
1177 Potential therapeutic targets. Biochem. Res. Int. *2012*, e248135.
1178 Yu, D., Swaroop, M., Wang, M., Baxa, U., Yang, R., Yan, Y., Coksaygan, T., DeTolla, L., Marugan, J.J., Austin,
1179 C.P., et al. (2014). Niemann-Pick Disease Type C: Induced Pluripotent Stem Cell-Derived Neuronal Cells
1180 for Modeling Neural Disease and Evaluating Drug Efficacy. J. Biomol. Screen. *19*, 1164–1173.
1181 Zhang, P., Kishimoto, Y., Grammatikakis, I., Gottimukkala, K., Cutler, R.G., Zhang, S., Abdelmohsen, K.,
1182 Bohr, V.A., Misra Sen, J., Gorospe, M., et al. (2019). Senolytic therapy alleviates Aβ-associated
1183 oligodendrocyte progenitor cell senescence and cognitive deficits in an Alzheimer's disease model.
1184 Nat. Neurosci. *22*, 719-728.